



Relativistic Components of the Ultra-fast Outflow in the Quasar PDS 456 from *Chandra*/HETGS, *NuSTAR*, and *XMM-Newton* Observations

Rozenn Boissay-Malaquin¹ , Ashkbiz Danehkar² , Herman L. Marshall¹ , and Michael A. Nowak^{1,3} 

¹Massachusetts Institute of Technology, Kavli Institute for Astrophysics, Cambridge, MA 02139, USA; rboissay@mit.edu

²Harvard-Smithsonian Center for Astrophysics, 60 Garden Street, Cambridge, MA 02138, USA

³Department of Physics, Washington University, One Brookings Drive, St. Louis, MO 63130-4899, USA

Received 2018 September 22; revised 2019 January 17; accepted 2019 January 19; published 2019 February 28

Abstract

We present the spectral analysis of *Chandra*/High Energy Transmission Grating Spectrometer (HETGS) and *NuSTAR* observations of the quasar PDS 456 from 2015, and *XMM-Newton* and *NuSTAR* archival data from 2013 to 2014, together with *Chandra*/HETGS data from 2003. We analyzed these three different epochs in a consistent way, looking for absorption features corresponding to highly ionized blueshifted absorption lines from H-like and He-like ions of iron (and nickel), as well as of other elements (O, Ne, Si, and S) in the soft band. We confirm the presence of a persistent ultra-fast outflow (UFO) with a velocity of $v_{\text{out}} = -0.24$ to $-0.29 c$, that has previously been detected. We also report the detection of an additional faster component of the UFO with a relativistic velocity of $v_{\text{out}} = -0.48 c$. We implemented photoionization modeling, using XSTAR analytic model `warmabs`, to characterize the physical properties of the different kinematic components of the UFO and of the partially covering absorber detected in PDS 456. These two relativistic components of the UFO observed in the three epochs analyzed in this paper are powerful enough to impact the host galaxy of PDS 456 through feedback from active galactic nuclei.

Key words: galaxies: active – galaxies: nuclei – quasars: absorption lines – X-rays: galaxies

1. Introduction

Outflows are commonly detected in active galactic nuclei (AGN) through absorption lines that are visible in X-rays and in the UV (Crenshaw et al. 2003) with a moderate velocity of hundreds to several thousands km s^{-1} . The so-called warm absorbers are found in more than 50% of AGN (Blustin et al. 2005; Piconcelli et al. 2005; McKernan et al. 2007). They are thought to result from efficient accretion onto supermassive black holes (SMBHs), if the radiative energy exceeds the binding energy of the gas (King & Pounds 2003; King 2010). Outflows with higher velocity ($v_{\text{out}} = -0.1$ to $-0.4 c$) that are also denser ($N_{\text{H}} \sim 10^{23} \text{ cm}^{-2}$) have also been observed through blueshifted iron absorption lines above 7 keV (Chartas et al. 2002; Reeves et al. 2009; Tombesi et al. 2010) in about 40% of AGN (Tombesi et al. 2010; Gofford et al. 2013), and in particular in bright and distant quasars (Chartas et al. 2003, 2014; Pounds et al. 2003; Reeves et al. 2003; Lanzuisi et al. 2012; Vignali et al. 2015; Dadina et al. 2018). These are often called ultra-fast outflows (UFOs). That they are so frequently detected suggests that they are characterized by a wide angle (e.g., Nardini et al. 2015; Reeves et al. 2018a). Their outflowing rates can reach several solar masses per year (up to $\sim 10^3 M_{\odot} \text{ yr}^{-1}$) for a kinetic power of 10^{45} – $10^{46} \text{ erg s}^{-1}$ (Reeves et al. 2009; Tombesi et al. 2011, 2013). The link between galaxy parameters and the growth of the central SMBH, such as the black hole mass—velocity dispersion M – σ relation (Ferrarese & Merritt 2000; Gebhardt et al. 2000), is thought to be regulated by AGN feedback processes via these powerful winds. The kinetic power of UFOs, launched from the accretion disk at a few gravitational radii (R_g) from the SMBH, can be 0.5%–5% of the bolometric luminosity, and can affect the AGN host galaxy by sweeping the galaxy reservoir of gas away, which quenches the star formation (Silk & Rees 1998; King & Pounds 2003; Di Matteo et al. 2005; Hopkins &

Elvis 2010; King 2010; Alexander & Hickox 2012; Fabian 2012; Kormendy & Ho 2013; Tombesi et al. 2015; Fiore et al. 2017). Several mechanisms have been suggested to play a role in the acceleration of these fast winds: UFOs can be radiatively driven winds (e.g., Proga & Kallman 2004; King 2010; Sim et al. 2010; Reeves et al. 2014; Hagino et al. 2015; King & Pounds 2015; Nomura & Ohsuga 2017), thermal winds (e.g., Begelman et al. 1983), or magnetohydrodynamic (MHD) flows (e.g., Blandford & Payne 1982; Fukumura et al. 2010, 2015, 2018a, 2018b; Chakravorty et al. 2016; Kraemer et al. 2018).

PDS 456, which was first identified by Torres et al. (1997) in the Pico dos Dias survey (PDS), is the most luminous radio-quiet quasar in the local universe ($z = 0.184$), with a bolometric luminosity of $L_{\text{Bol}} = 10^{47} \text{ erg s}^{-1}$ (Reeves et al. 2000) and a black hole mass of $M_{\text{BH}} = 10^9 M_{\odot}$ (Reeves et al. 2009). Its initial observations were taken with *RXTE*, *ASCA*, *BeppoSAX*, and then *XMM-Newton* (Reeves et al. 2000; Vignali et al. 2000; Reeves et al. 2002), and have shown a steep absorption feature around 9 keV, as well as a rapid variability, suggesting the presence of an absorbing highly ionized outflow in the line of sight. The deep absorption trough detected above 7 keV has been associated with the blueshifted K-shell transition of highly ionized iron (Fe XXVI). Broad absorption features in *XMM-Newton*/RGS data near 1 keV are additional signatures of a dense and highly ionized UFO with an extreme velocity of about $v_{\text{out}} = -0.1$ to $-0.2 c$ (Reeves et al. 2003; Behar et al. 2010).

This persistent UFO was also identified in *Suzaku* observations via an absorption feature near 9 keV that corresponds to a Compton-thick and clumpy wind of velocity $v_{\text{out}} = -0.25$ to $-0.30 c$ (Reeves et al. 2009). The rapid variability of the high-velocity iron K-shell absorption lines may result from wind clumpiness (Gofford et al. 2014; Reeves et al. 2016). The spectral variability of PDS 456 can be explained by the variations in the partially covering absorber that is observed in

most of the data (e.g., Reeves et al. 2014, 2016; Nardini et al. 2015; Matzeu et al. 2016a; see also the principal component analysis, PCA, performed by Parker et al. 2018 on *XMM-Newton* and *Suzaku* data). In this model, the clouds responsible for the partial covering have a size of $20 R_g$ and would be the denser clumps of the inhomogeneous accretion disk wind (Matzeu et al. 2016b; Reeves et al. 2018a). Luminari et al. (2018) have recently determined that the $0.23c$ -velocity wind may be a wide-angle outflow, according to the covering factor of 0.7 and the opening angle of 71° that results from the application of an AGN wind emission model (WINE) to *XMM-Newton* and *NuSTAR* data.

Nardini et al. (2015) analyzed five simultaneous *XMM-Newton* and *NuSTAR* observations from 2013 to 2014 and found in all these observations a broadened Fe K emission line in addition to an absorption trough that they first fit with individual lines and then with a P Cygni profile, which is characteristic of a spherically symmetric expanding gas. Their analysis revealed for the first time several blueshifted absorption lines (Fe XXVI $Ly\alpha$, $Ly\beta$, and K edge) with the same outflow velocity $v_{\text{out}} = -0.25 c$. Nardini et al. (2015) performed photoionization modeling of PDS 456 using the photoionization program XSTAR (Kallman & Bautista 2001), constrained with its spectral energy distribution (SED) based on data from UV to hard X-rays (from 2 eV to 30 keV) collected by *NuSTAR* and *XMM-Newton* EPIC-*pn* and *OM* observations from 2013 to 2014, approximated by a three-segment broken power law (Nardini et al. 2015). The hard X-ray power law has a photon index of $\Gamma = 2.4$ according to *XMM-Newton*/EPIC and *NuSTAR* data. The *OM* photometric data are well described by a slope of $\Gamma = -0.7$, the connecting slope between 10 and 500 eV being $\Gamma = 3.3$. A more complex description of this SED with a multi-temperature Comptonized accretion disk model was applied by Matzeu et al. (2016b) to *Suzaku* data. An analysis of the *RGS* data was performed by Reeves et al. (2016), who found broad absorption line (BAL) profiles at around 1 keV, which they identified as He- and H-like neon and L-shell iron lines that are blueshifted by a velocity of $v_{\text{out}} = -0.1$ to $-0.2 c$, which could be the signature of a lower ionization and clumpy phase of the accretion disk wind that is responsible for the absorption trough around 9 keV. The emission lines detected by Nardini et al. (2015), Reeves et al. (2016), and Matzeu et al. (2017a) in *Suzaku* data are likely associated with the reemission from the outflow in PDS 456. Reflection on ionized material has also been considered in several studies, but the scenario of an ultra-fast outflow absorbing the hot corona emission was often preferred (Reeves et al. 2009, 2014; Behar et al. 2010; Nardini et al. 2015; Chiang et al. 2017).

Broad absorption line profiles are expected in the UV spectrum of PDS 456 as signatures of the fast outflowing gas detected in X-rays. O’Brien et al. (2005) indeed detected a $Ly\alpha$ BAL in the UV spectrum of the *Hubble Space Telescope* (*HST*), blueshifted with a velocity of $v_{\text{out}} = -0.05$ to $-0.08 c$, which could be the signature of a decelerating cooling outflow. However, a recent analysis of the same data by Hamann et al. (2018) identified this UV BAL as a C IV line blueshifted with a velocity of $v_{\text{out}} = -0.3 c$, similar to the one measured in X-ray data. This BAL could come from dense and low-ionization clumps embedded in the X-ray UFO.

Considering the fact that the SMBH in PDS 456 is accreting at about the Eddington limit, its detected UFO should be radiatively driven (Nardini et al. 2015; Matzeu et al. 2017b). This is supported by a correlation between the velocity of the outflow and the ionizing luminosity, with the UV line driving strongly contributing to the wind acceleration (Hagino et al. 2015; Hamann et al. 2018; Reeves et al. 2018a). However, an MHD-wind model has also recently been successfully applied to *XMM-Newton* and *NuSTAR* data of PDS 456 by Fukumura et al. (2018b).

Despite the fact that PDS 456 is a radio-quiet quasar, it has recently been observed by the European VLBI Network at 5 GHz (Yang et al. 2019). This observation revealed a radio structure made of two components, which are faint, diffuse, and separated by about 20 pc. They could either be the signature of a recent jet or the radio emission of an outflow launched in the vicinity of the central SMBH. In the latest hypothesis, the radio emission could originate from shocks produced by the interaction of the known powerful mildly relativistic X-ray outflow and the surrounding material.

Recent observations with *XMM-Newton* and *NuSTAR* in 2017 have shown the presence of an additional faster UFO with a velocity of $v_{\text{out}} = -0.46 c$, identified from a deep absorption line around 11 keV, which may be part of the multiple velocity components of the UFO around the accretion disk, launched from a radius of about $10R_g$, and may be visible only during the lowest states (Reeves et al. 2018a, 2018b). In addition to the two fast components of the UFO, a less strongly ionized soft absorber with a variable covering factor was detected, which probably originates from denser clumps farther out along the stratified outflow (Reeves et al. 2018a). Simultaneous UV data from *HST* did not show a significant absorption signature because the X-ray absorbers might be too highly ionized to be visible in this energy band.

In the present paper, we aim to analyze multiple epochs of PDS 456, namely *Chandra*/High Energy Transmission Grating Spectrometer (HETGS) data (from 2003 and 2015), *NuSTAR* data (from 2015), and *XMM-Newton* and *NuSTAR* data from 2013 to 2014, to look for signatures of the persistent UFO that has previously been detected and of the faster UFO that has recently been identified, and constrain their physical properties. We describe the data, their selection, and their reduction in Section 2. We then present our dual-approach spectral analysis. We first explain the combination and binning of the data in Section 3.1 and the continuum fitting in Section 3.2. We next present a model-independent analysis, involving the modeling of the absorption features at high energy with Gaussian lines (Section 3.3) and with P Cygni profiles (Section 3.4). We finally present in Section 3.5 the model-dependent approach that consists of photoionization modeling, before we discuss the results in Section 4. We conclude in Section 5.

2. Data

2.1. Data Selection

The aim of this work is to look for signatures of UFOs in PDS 456. For this purpose, we chose to focus on three different data sets, as presented in Table 1. The strongest

Table 1
Observation Log

Label	Instrument	Obs. ID	Obs. Start	Obs. End	T_{tot}	T_{net}	Channel	Count Rate	Flux
CN	<i>Chandra</i> /HETGS	17452	2015 Jul 21, 12:52	2015 Jul 23, 03:48	138	136	HEG	0.098	5.16 ± 0.07
							MEG	0.100	6.00 ± 0.12
	<i>NuSTAR</i>	90101008002	2015 Jul 21, 11:01	2015 Jul 23, 07:46	160	74	FPMA	0.048	4.63 ± 0.14
							FPMB	0.044	4.51 ± 0.16
		90101008004	2015 Jul 24, 11:36	2015 Jul 25, 10:51	83	38	FPMA	0.044	4.75 ± 0.81
							FPMB	0.042	4.47 ± 0.20
C	<i>Chandra</i> /HETGS	4063	2003 May 7, 03:29	2003 May 8, 20:08	145	143	HEG	0.070	3.85 ± 0.06
							MEG	0.073	4.23 ± 0.07
XN1	<i>XMM-Newton</i>	0721010201	2013 Aug 27, 04:41	2013 Aug 28, 11:13	110	85.5	EPIC/pn	3.175	10.87 ± 0.04
							<i>NuSTAR</i>	60002032002	2013 Aug 27, 03:41
							FPMB	0.128	9.50 ± 0.23
							<i>XMM-Newton</i>	0721010301	2013 Sep 6, 03:24
XN2	<i>XMM-Newton</i>	0721010301	2013 Sep 6, 03:24	2013 Sep 7, 10:36	112	92.1	EPIC/pn	2.098	5.63 ± 1.39
							<i>NuSTAR</i>	60002032004	2013 Sep 6, 02:56
							FPMB	0.049	3.61 ± 0.17
							<i>XMM-Newton</i>	0721010401	2013 Sep 15, 18:47
XN3	<i>XMM-Newton</i>	0721010401	2013 Sep 15, 18:47	2013 Sep 17, 03:57	119	102.0	EPIC/pn	1.974	6.08 ± 0.02
							<i>NuSTAR</i>	60002032006	2013 Sep 15, 17:56
							FPMB	0.068	4.59 ± 0.18
							<i>XMM-Newton</i>	0721010501	2013 Sep 20, 02:47
XN4	<i>XMM-Newton</i>	0721010501	2013 Sep 20, 02:47	2013 Sep 21, 09:37	111	92.9	EPIC/pn	1.925	6.35 ± 0.03
							<i>NuSTAR</i>	60002032008	2013 Sep 20, 03:06
							FPMB	0.073	5.38 ± 0.17
							<i>XMM-Newton</i>	0721010601	2014 Feb 26, 08:03
XN5	<i>XMM-Newton</i>	0721010601	2014 Feb 26, 08:03	2014 Feb 27, 22:51	140	103.9	EPIC/pn	1.383	4.47 ± 1.38
							<i>NuSTAR</i>	60002032010	2014 Feb 26, 08:16
							FPMB	0.043	3.00 ± 0.58

Note. Summary of PDS 456 *Chandra*, *XMM-Newton*, and *NuSTAR* observations used in this study. Observation CN considers the contemporaneous observations with *Chandra*/HETGS and *NuSTAR* from 2015, while observation C refers to the archival *Chandra*/HETGS observation from 2003. Observations XN1 to XN5 refer to *XMM-Newton* and *NuSTAR* observations performed in 2013–2014 and previously analyzed by Nardini et al. (2015). We refer to the combination of observations XN1 to XN5 as observation XN. Observation start and end times are in UT. T_{tot} (in ks) is the total elapsed time, while T_{net} (in ks) is the net exposure after screening and deadtime correction. The count rates (in s^{-1}) are the background-subtracted count rates. The fluxes (in 10^{-12} erg cm^{-2} s^{-1}) refer to the 0.8–7 keV (HEG), 0.4–7 keV (MEG), 0.4–10 keV (EPIC/pn) and 3–30 keV (FPMA/FPMB) bands, obtained using the ISIS function `data_flux()`, which calculates the absorbed X-ray flux solely from the spectral data, and estimates errors from the data and information from the instrumental responses.

signatures of UFOs are found at high energy, above 7 keV, as found in particular in PDS 456, according to previous studies. We thus selected observations including *NuSTAR* data, namely *XMM-Newton* and *NuSTAR* data from 2013 to 2014 (observations “XN”), and *Chandra* and *NuSTAR* data from 2015 (observation “CN”). Other signatures of the UFOs are expected at lower energy, so *Chandra*/HETGS is an excellent instrument to look for such features. We also considered *Chandra*/HETGS data from 2003 (observation “C”), data that together with CN data have never been analyzed in detail. Despite the lack of high-energy data for this C observation, our analysis, which is performed consistently along the different data sets, allowed us to constrain the wind parameters in this observation as well. For observations XN, we focused on EPIC/pn data, mostly to look for high-energy signatures of the UFOs. We did not reanalyze *RGS* data, which have already been studied in detail by Reeves et al. (2016), because we focus on high-velocity and high-ionization outflows whose signatures are expected to be beyond the energy range of *RGS*. The scope of

the present paper is to look for signatures of UFOs at both high and low energies, so we did not examine other archival data.

2.2. Data Reduction

PDS 456 was observed with the HETGS (Markert et al. 1994; Canizares et al. 2005) using the *Chandra* Advanced CCD Imaging Spectrometer (ACIS; Garmire et al. 2003), from 2015 July 21 to July 23 (observation CN, 138 ks of exposure time, see Table 1) and from 2003 May 07 to 08 (observation C, 145 ks of exposure time, see Table 1). The HETGS spectrometer is composed of two grating types: the medium-energy gratings (MEGs), covering the 0.4–7 keV energy band, with an FWHM resolution of 0.023 Å, and the high-energy gratings (HEGs), having an FWHM resolution of 0.012 Å in the 0.8–10 keV band. Data processing was performed with the TGCat software (Huenemoerder et al. 2011), which employs *Chandra* Interactive Analysis of Observations tools (CIAO v.4.8; Fruscione et al. 2006) and

Calibration Data base (CALDB v.4.8.0). *Chandra*/HETGS data for both periods were reduced in a standard way, using a narrow mask to avoid mask confusion above 6 keV. Plus and minus first-order ($m = \pm 1$) MEG and HEG data were extracted from the -1 and the $+1$ arms of the MEG and HEG gratings for the source and the background for both observations, using the CIAO tool `tgextract`. Spectral redistribution matrix files and effective area files were generated with `mkgrmf` and `mkgarf`.

PDS 456 was simultaneously observed by *NuSTAR* during observation CN of *Chandra*, from 2015 July 21 to 23 (74 ks exposure) and from July 24 to 25 (38 ks exposure). *NuSTAR* data were processed using the NuSTARDAS v1.7.1. The source spectra were extracted using a $45''$ circular region centered on the source, and the background from a $45''$ circular region clear of straylight in the same detector for both focal plane modules A and B (FPMA and FPMB). Observation reports depict a notable solar activity, which may impact the background event rate during both *NuSTAR* observations. Passage of solar coronal mass ejections over the Earth induces a temporary increase in the low Earth orbit radiation environment (which can persist for many orbits) and can significantly increase the background event level in the detectors of *NuSTAR* when the observatory is close to the South Atlantic Anomaly (SAA). We thus optimized the screening out of high-background periods near SAA passages using the module `nucalcsaa`.

PDS 456 was observed in 2013–2014 by *NuSTAR* and by *XMM-Newton* in five observations labeled XN1 to XN5 in Table 1 (see Nardini et al. 2015). We reduced the *NuSTAR* observations as described above, filtering the SAA passages when required, in order to compare our results to previous observations. We also reduced the *XMM-Newton* original data files using the *XMM-Newton* Standard Analysis Software (SAS v16.0.0 - Gabriel et al. 2004) considering the EPIC/pn (Strüder et al. 2001) spectrum for each observation of PDS 456. Events corresponding to flaring particle background were filtered using the SAS standard procedure. Single and double events were selected for extracting spectra. The data were screened for any increased flux of background particles. Spectra were extracted from a circular region of $30''$ centered on the source. We checked for pile-up in all observations. The background was extracted from a nearby source-free region of $40''$ in the same CCD as the source. Response matrices were generated for each source spectrum using the SAS `arfgen` and `rmfgen` tasks.

3. Spectral Analysis

We performed our dual-approach spectral analysis of the data listed in Table 1 using the Interactive Spectral Interpretation System (ISIS; version 1.6.2-40, Houck 2002). We analyzed the simultaneous data from *Chandra*/HETGS and *NuSTAR* from 2015 (observation CN), the simultaneous time-averaged *XMM-Newton* and *NuSTAR* observation (combined data XN1 to XN5), and the archival *Chandra*/HETGS observation from 2003 (observation C) in a similar way, adapting the procedure to the available data sets, as described in the following. After describing the combination and binning of our data in Section 3.1 and the continuum modeling in Section 3.2, we perform a model-independent analysis of the selected observations, looking at individual

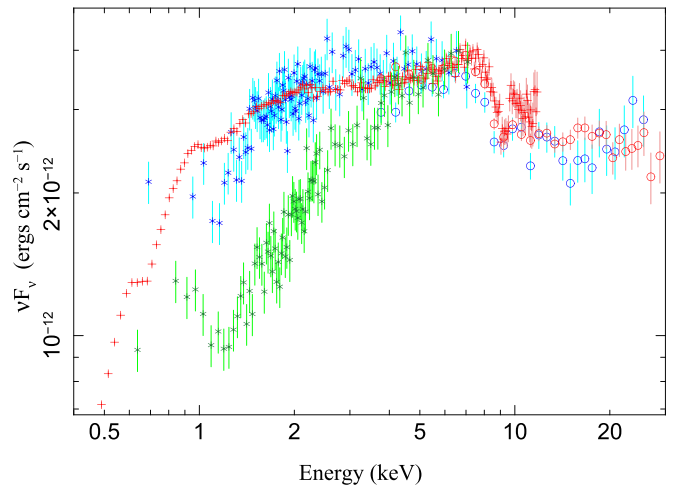


Figure 1. Unfolded spectra of the three observations studied in this paper (see Table 1). Blue: observation CN. Red: observation XN. Green: observation C. Symbols: a cross stands for HETGS data, an empty circle for *NuSTAR* data, and a plus for EPIC/pn data. Note that the spectra have been strongly rebinned for plotting purposes.

features at high energy (Sections 3.3 and 3.4) and in the broadband spectra (the blind line search is described in the appendix). We then perform a model-dependent analysis using photoionization modeling (Section 3.5). This dual-method involving both model-dependent and model-independent analyses is an accurate way to check that the results found via different procedures are consistent and thus reliable. In this paper, all errors are quoted at 1σ confidence level. All figures are presented in rest-frame energy. Figure 1 shows the spectra of the three observations (coarsely rebinned for presentation purposes), and illustrates the changes in fluxes and shapes between the different epochs, as has been noted in previous studies (e.g., Matzeu et al. 2017b).

3.1. Combination and Binning

In order to increase the signal-to-noise ratio and because of the complex shape of the broadband spectrum around 9 keV (as described in Section 1), we combined the data to perform the spectral analysis, using the `combine_data` sets function in ISIS. For observation CN (see Table 1), we placed the HEG data on the same grid as MEG and combined all HETGS spectra (HEG-1, HEG+1, MEG-1, and MEG+1), and we also combined *NuSTAR* FPMA and FPMB data of the two observations 90101008002 and 90101008004. We used a combination of binning by signal-to-noise ratio and channel binning in order to obtain an adequate signal-to-noise ratio even below 1 keV (as discussed by Danehkar et al. 2018). We have thus binned *Chandra* and *NuSTAR* data with a minimum of one channel per bin (binned to the half-width at half-maximum of the MEG resolution) and a minimum signal-to-noise ratio of 2. We took into account the background. The same binning as for *Chandra* data has been used for observation C. As our C and CN observations have a Poisson distribution, we used Cash statistics (Cash 1979) to analyze these data. To estimate the error bars and evaluate the significance of our results, we used a ΔC value, which is appropriate for a likelihood estimate with Poisson statistics

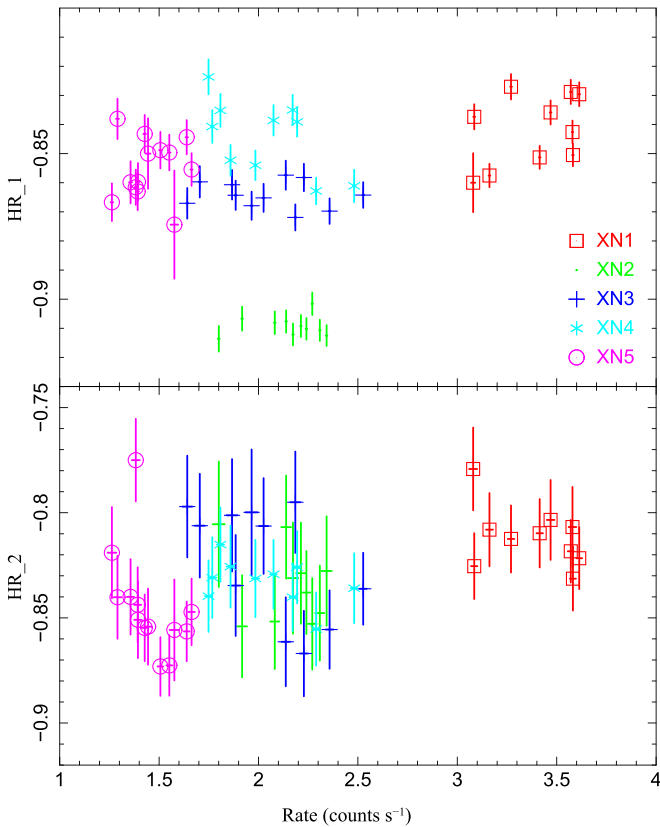


Figure 2. Hardness ratios defined in Equations (1) and (2) for the five XN observations, plotted against the 0.5–10 keV EPIC/pn light curve. HR_1 is sensitive to the overall continuum shape; the top panel shows that this shape is consistent for all XN observations except for the second observation, which is slightly softer. HR_2 is sensitive to the slope of the spectrum around the 8–15 keV region and is generally consistent between these XN observations.

(corresponding to a given confidence level and a given number of degrees of freedom) that is analogous to $\Delta\chi^2$ for the case of Gaussian statistics (see, e.g., the statistical textbook from Breiman 1973, works from Cash 1979 and Wilks 1938, and the pedagogical discussions in Arnaud et al. 2011).

For the simultaneous *XMM-Newton* and *NuSTAR* data set, we combined the *pn* spectra of the five observations XN1 to XN5, as well as the FPMA and FPMB spectra. We refer to this combined data set as XN. Despite the significant variability in the shape of the spectra that was described by Nardini et al. (2015), this combination of data is possible because of compatible fluxes for each observation, and because the absorption through around 9 keV is detected in all observations with similar parameters. We calculated the hardness ratios of the five observations (see Figure 2) using count rates CR in different energy bands:

$$HR_1 = \frac{CR_{5-10 \text{ keV}}^{XMM} - CR_{0.5-4 \text{ keV}}^{XMM}}{CR_{5-10 \text{ keV}}^{XMM} + CR_{0.5-4 \text{ keV}}^{XMM}}, \quad (1)$$

and

$$HR_2 = \frac{CR_{15-30 \text{ keV}}^{NuSTAR} - CR_{3-8 \text{ keV}}^{XMM}}{CR_{15-30 \text{ keV}}^{NuSTAR} + CR_{3-8 \text{ keV}}^{XMM}}, \quad (2)$$

in order to study the possible impact of spectral changes among the observations. By their definitions, HR_1 gives information

about spectral variability regarding the whole EPIC/pn energy band, while HR_2 represents the variability of the continuum shape around the absorption features at 9 and 11 keV. In the top panel of Figure 2, the hardness ratio of the second XN observation is slightly lower, which is due to a small change in the spectral shape of the EPIC/pn spectrum, as shown in Figure 1 from Nardini et al. (2015). However, by comparing the spectra resulting from the sum of XN observations with and without this second observation, we did not notice any significant change in the spectral shape. In the bottom panel of Figure 2, we see that the hardness ratio that is representative of the variability around the absorption features is consistent among the five XN observations. The hardness ratios presented in Figure 2 show that all XN observations are consistent spectrally and can be combined for our analysis. The stability of HR_2 shows that the absorption features around 9 and 11 keV are not due to changes of the continuum. We thus combined the data in order to increase the signal-to-noise ratio and to obtain an average shape of the P Cygni-like profile that is detected in individual observations, which is to be compared with the CN observation. We binned *NuSTAR* data to a minimum of two channels per bin and a minimum signal-to-noise ratio of 2, and *XMM-Newton* data to a minimum of one channel per bin and a minimum signal-to-noise ratio of 5 (during the analysis described in the following sections, we checked that rebinning the data to a minimum of five channels per bin does not change the results on the absorption lines). The binning of these data is sufficient to obtain enough counts per channel to allow us to use χ^2 statistics for the analysis.

3.2. Continuum Modeling

To perform a precise analysis of the combined data sets described above, in particular the absorption features, we needed to determine the continuum carefully. Following the modeling of the continuum performed in previous studies, and in particular by Nardini et al. (2015), on the same *XMM-Newton* and *NuSTAR* data, we first determined the continuum for observation CN. We thus first fit the hard-energy band above 3 keV with a simple power law, taking into account Galactic absorption (with $N_{\text{H}}^{\text{gal}}$ fixed to $2.4 \times 10^{21} \text{ cm}^{-2}$ according to 21 cm measurements, Dickey & Lockman 1990; Kalberla et al. 2005), modeled with the `tbabs` absorption model (Wilms et al. 2000). We used a cross-calibration factor to allow us to simultaneously fit data from different satellites, but the photon index of the power law was the same. The fit resulted in a C statistic of 472.8 for 364 dof. In order to account for the spectral curvature, which has been found in previous studies to range between 2 and 5 keV (e.g., Reeves et al. 2009, 2014, 2018a; Turner & Miller 2009; Behar et al. 2010), we added a partially covering absorption to the power law using the `zpcfabs` model, which improved the fit significantly, with a ΔC of 15.4 (for two parameters of interest) and an ftest F-value of 4.05 and a p-value of 0.007. This partial covering by a moderately ionized absorber could well describe the continuum spectral variability, due to patchy obscuration, e.g., in NGC 5548 (Kaastra et al. 2014) or NGC 3516 (Turner et al. 2011). We also checked for the presence of neutral distant reflection by replacing the simple power law with a `pexmon` model. However, the improvement of the fits is less significant,

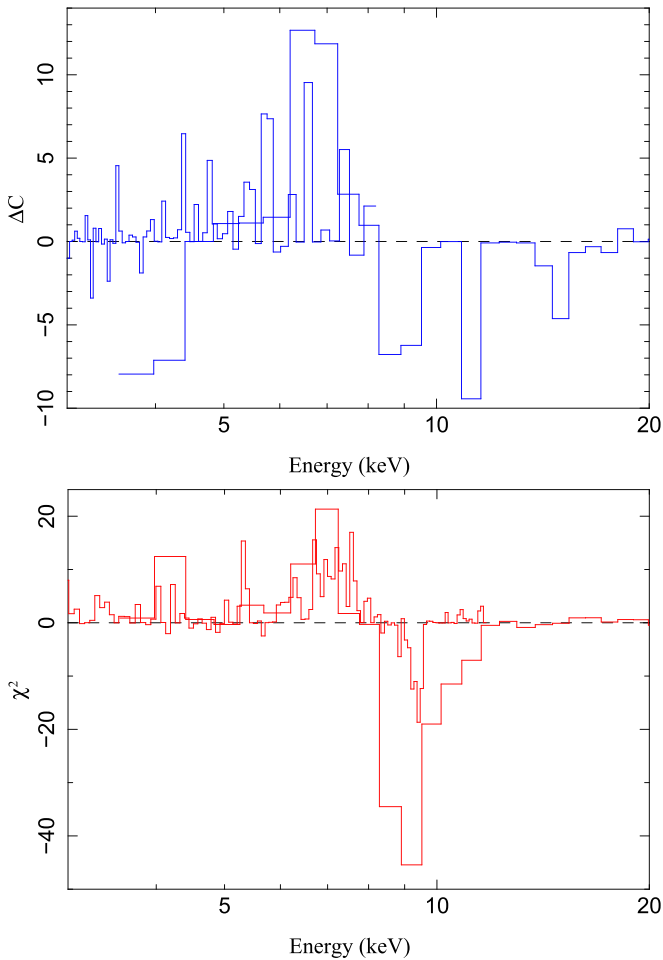


Figure 3. Ratio between the data and their corresponding continuum model between 3 and 20 keV. Top panel (blue): data-to-model ratio for observation CN, expressed as ΔC . Bottom panel (red): data-to-model ratio for observation XN, expressed as $\Delta\chi^2$. Note that the spectra have been strongly rebinned for plotting purposes.

with a ΔC of 11.1 (for three free parameters), an F-value of 2.97, but a p-value of 0.03. Furthermore, the spectra of our data sets do not show an excess around 30 keV or a fluorescence of the Fe $K\alpha$ line at 6.4 keV. The spectral complexity of our data sets above 3 keV is well illustrated by the data-to-model ratios of observations CN and XN in Figure 3.

When the soft part of the spectra is added and the continuum model determined in hard X-rays is extrapolated in the soft band, we clearly detect a soft excess below 1 keV, as well as strong emission and absorption features, mostly broadened, especially around 1 keV and above 7 keV (QSO frame energy). We modeled the soft excess with a broad Gaussian emission line (*zgauss*), that is, with a phenomenological model. We chose to fit the soft excess with a broad line to be consistent with the analysis from Nardini et al. (2015; because we reanalyzed the same data) and because using a more common blackbody component instead did not improve the fit. The resulting continuum model is

$$\text{cst} * \text{tbabs} * \text{zpcfabs} * (\text{power law} + \text{zgauss}) .$$

As the continuum model of observation CN is totally consistent with the analysis of *XMM-Newton* and *NuSTAR* data

Table 2
Continuum Parameters

Parameters	Obs. CN	Obs. XN	Obs. C
Power law:			
Photon index	$2.30^{+0.0048}_{-0.012}$	$2.33^{+0.009}_{-0.008}$	$2.47^{+0.01}_{-0.01}$
$F_{7-30\text{keV}}$	$1.28^{+0.011}_{-0.011}$	$1.24^{+0.001}_{-0.001}$	$1.27^{+0.013}_{-0.013}$
$F_{0.4-30\text{keV}}$	$12.27^{+0.10}_{-0.10}$	$13.31^{+0.0015}_{-0.0015}$	$16.49^{+0.16}_{-0.16}$
Partial covering:			
N_{H}	$3.03^{+0.46}_{-0.53}$	$8.46^{+0.49}_{-0.42}$	$3.42^{+0.14}_{-0.11}$
Covering factor	$0.32^{+0.009}_{-0.006}$	$0.33^{+0.009}_{-0.009}$	$0.75^{+0.004}_{-0.004}$
Soft excess:			
E	$0.060^{+0.008}_{-0.01}$	$0.69^{+0.007}_{-0.007}$	$0.14^{+0.05}_{-0.03}$
σ	$0.10^{+0.0017}_{-0.0017}$	$0.19^{+0.004}_{-0.004}$	$0.06^{+0.003}_{-0.006}$
$F_{0.4-30\text{keV}}$	$65.59^{+13.67}_{-15.45}$	$0.97^{+0.007}_{-0.007}$	$9.43^{+3.44}_{-2.87}$
Cross-calibration	$0.90^{+0.005}_{-0}$	$0.97^{+0.007}_{-0.007}$...
C or χ^2/dof	1693.48/1609	2240.58/1704	1409.60/1331

Note. Parameters of the continuum fit, performed above 0.4 keV, for the three observations, as described in Section 3.2. Fluxes are in units of 10^{-12} erg s^{-1} cm^{-2} .

from Nardini et al. (2015), we applied it to our combined XN data. In order to analyze all our observations in a similar way, we also applied this model to our C observation, for which the continuum is determined on a smaller energy band. The parameters of the broadband fitting with this continuum model are given in Table 2.

3.3. Fe K Emission and Absorption Features

After establishing the continuum model, we looked for absorption features above 7 keV. We fit the spectra above 3 keV, adding Gaussian and edge models to the base continuum model in order to constrain the emission and absorption profiles in the Fe–K band, similarly to Nardini et al. (2015). We first added *gabs* lines, one in emission (using a negative normalization) and two in absorption, and an edge, in order to account for the Fe XXVI $\text{Ly}\alpha$ emission and absorption lines (at $E_{\text{lab}} = 6.97$ keV), the Fe XXVI $\text{Ly}\beta$ absorption line (at $E_{\text{lab}} = 8.25$ keV) and the Fe XXVI K edge (at $E_{\text{lab}} = 9.28$ keV). We tied the widths and shifts of the absorption lines together. The width and shift of the emission line were also free to vary, independently of those of the absorption features. In this way, we were able to measure the outflow velocities of the UFO in emission and in absorption. We performed this fit for both CN and XN observations because the *NuSTAR* data helped so well to define the continuum. The significance of each line is given by ΔC for observation CN and $\Delta\chi^2$ for observation XN, first adding the emission line to the continuum (with three parameters of interest), then the $\text{Ly}\alpha$ absorption line (three free parameters), then the $\text{Ly}\beta$ absorption line (linked in shift and width, so only one free parameter), and finally the edge (linked in shift, leaving one parameter of interest). The parameters of this fit are shown in Table 3. Our results show that the Fe XXVI $\text{Ly}\alpha$ emission and absorption line are significantly detected, in addition to the Fe XXVI $\text{Ly}\beta$ absorption line and the Fe XXVI K edge (at lower significance), with a slight emission blueshifted by -0.01 to $-0.02 c$ and a large absorption blueshift of $-0.27c$. Note that we assessed the

Table 3
Fits Performed above 3 keV with One Set of Fe Lines

Parameters		Obs. CN			Obs. XN		
Line		E_{rest} (keV)	EW (eV) or τ	$\Delta C/\Delta\text{dof}$	E_{rest} (keV)	EW (eV) or τ	$\Delta\chi^2/\Delta\text{dof}$
Fe XXVI Ly α	em.	7.04	233^{+46}_{-46}	28.28/3	7.13	91^{+16}_{-16}	96.50/3
	abs.	9.16	259^{+71}_{-71}	15.55/3	9.15	212^{+23}_{-23}	134.18/3
Fe XXVI Ly β abs.		10.84	142^{+88}_{-88}	3.09/1	10.83	132^{+29}_{-29}	23.58/1
Fe XXVI K edge		12.20	$0.10^{+0.05}_{-0.05}$	4.31/1	12.18	$0.06^{+0.03}_{-0.03}$	5.06/1
v_{out}/c	em.		$-0.010^{+0.02}_{-0}$			$-0.022^{+0.012}_{-0.012}$	
	abs.		$-0.267^{+0.0312}_{-0.023}$			$-0.266^{+0.0051}_{-0.0052}$	
σ (keV)	em.		$0.600^{+0}_{-0.0791}$			$0.442^{+0.0874}_{-0.0769}$	
	abs.		$0.457^{+0.1432}_{-0.1568}$			$0.319^{+0.0423}_{-0.0390}$	
C or χ^2/dof		379.09/358 = 1.059			1150.37/1179 = 0.9757		

Note. Energies are in keV, velocities in units of c , and line widths σ are in keV. The equivalent width (EW, in eV) and the depth τ give information about the strength of the Gaussian line (in the first case) and of the edge (in the second case). The significance of each line is given by ΔC or $\Delta\chi^2$.

Table 4
Fits Performed above 3 keV with Two Sets of Fe Lines

Parameters		Obs. CN			Obs. XN		
Line		E_{rest} (keV)	EW (eV) or τ	$\Delta C/\Delta\text{dof}$	E_{rest} (keV)	EW (eV) or τ	$\Delta\chi^2/\Delta\text{dof}$
UFO 1&2	Fe XXVI Ly α em.	7.11	233^{+46}_{-46}	27.19/3	7.13	97^{+15}_{-15}	104.29/3
UFO 1	Fe XXVI Ly α abs.	9.05	231^{+59}_{-59}	16.29/3	9.13	159^{+18}_{-18}	126.36/3
	Fe XXVI Ly β abs.	10.71	46^{+0}_{-0}	-0.58/1	10.80	432^{+11}_{-11}	1.89/1
	Fe XXVI K edge	12.04	$0.052^{+0.042}_{-0.080}$	1.36/1	12.15	$0^{+0.012}_{-0}$...
UFO 2	Fe XXVI Ly α abs.	11.50	161^{+76}_{-76}	9.61/3	11.59	161^{+57}_{-57}	28.68/3
	Fe XXVI Ly β abs.	13.62	161^{+129}_{-129}	2.98/1	13.72	161^{+77}_{-77}	5.18/1
	Fe XXVI K edge	15.32	$0.021^{+0.011}_{-0.062}$	0.09/1	15.43	$0^{+0.005}_{-0}$...
UFO 1&2	v_{out}/c em.		$-0.020^{+0.0229}_{-0}$			$-0.023^{+0.0114}_{-0.0033}$	
UFO 1	v_{out}/c abs.		$-0.255^{+0.021}_{-0.019}$			$-0.263^{+0.0049}_{-0.0050}$	
UFO 2	v_{out}/c abs.		$-0.463^{+0.006}_{-0.016}$			$-0.469^{+0.0321}_{-0.0279}$	
UFO 1&2	σ (keV) em.		$0.600^{+0}_{-0.071}$			$0.449^{+0.0808}_{-0.0710}$	
UFO 1	σ (keV) abs.		$0.472^{+0.128}_{-0.131}$			$0.282^{+0.0462}_{-0.0438}$	
UFO 2	σ (keV) abs.		$0.100^{+0.060}_{-0}$			$0.560^{+0.0400}_{-0.2465}$	
C or χ^2/dof		372.95/353 = 1.057			1137.82/1174 = 0.9692		
ΔC or $\Delta\chi^2/\Delta\text{dof}$		6.14/5			12.55/5		

Note. Parameters are defined as in Table 3. The last line of the table shows the significance of the fit improvements when the second UFO is considered in addition to the first.

statistical significance of the lines using $\Delta\chi^2$ and ΔC , but this method only gives an approximated significance according to Protassov et al. (2002).

In order to assess the presence of a second higher-velocity UFO as claimed by Reeves et al. (2018b), we added a second set of absorption lines (using two additional absorption Gaussian lines and another edge), with linked widths and shifts, these parameters being allowed to be different from those of the first UFO and of the emission component. The parameters of this fit are shown in Table 4. The results show that the Fe XXVI Ly α emission and absorption lines for both

UFOs ($v_{\text{out}1} = -0.26 c$ and $v_{\text{out}2} = -0.47 c$) are detected significantly, the Fe XXVI Ly β absorption line from the second UFO being detected at a lower confidence level. However, the Fe XXVI Ly β absorption line of the first UFO and the Fe XXVI K edges of both winds are not detected significantly. Furthermore, the width of the lines from the second UFO is hardly constrained in observation CN because it can only be established from *NuSTAR* data that have a lower spectral resolution than data from *XMM-Newton*. Considering the improvement of the fit when taking into account the second UFO, looking at the statistics (last line of Table 4), and at the

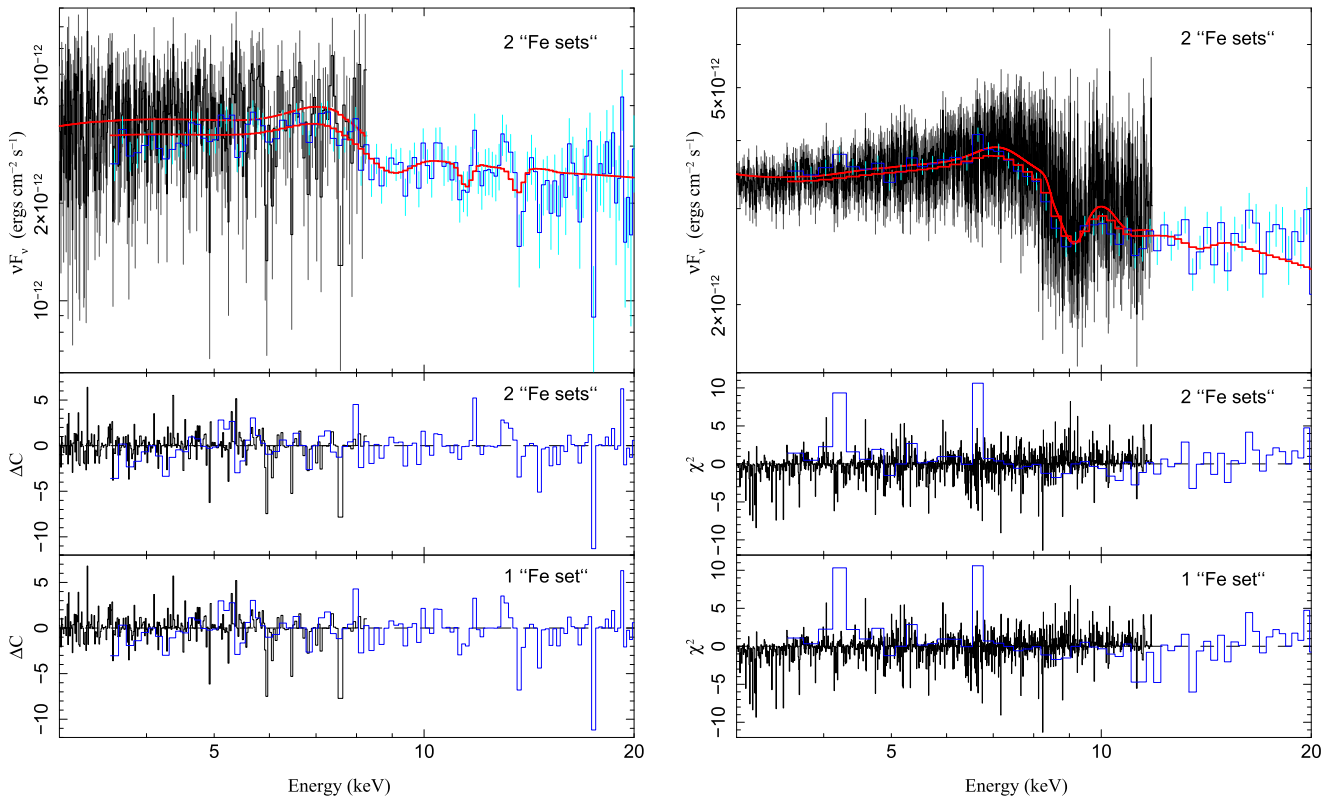


Figure 4. Unfolded hard spectra and residuals of observations CN (left) and XN (right) fit above 3 keV with two sets (top and middle panels) or one (bottom panel) set of Fe lines (corresponding to two UFOs or one UFO, as described in Section 3.3). We especially note the improvement on the residuals above 10 keV when the second UFO is taken into account.

residuals (in Figure 4), we assess that a second faster UFO is required by the data, significantly for observation XN (at about 97% confidence level), but only marginally for observation CN (slightly above 1σ confidence level).

3.4. P Cygni-like Profiles

The combination of the broad emission and the broad and blueshifted absorption Fe XXVI line has a P Cygni-like profile that is associated with the expansion of spherically symmetric stellar winds. Similarly to Nardini et al. (2015), we applied a model from Done et al. (2007), based on the Sobolev approximation with exact integration (SEI; Lamers et al. 1987), to reproduce Fe–K absorption features in this object. The velocity field $w = v/v_\infty$, i.e., the ratio between the wind velocity v and the terminal velocity v_∞ , is defined in the model by $w = w_0 + (1 - w_0)(1 - 1/x)^\gamma$, with w_0 the velocity at the photosphere and $x = r/R_0$ the radial distance r normalized to the photospheric radius R_0 . The optical depth of the line is described by $\tau(w) \approx \tau_{\text{tot}} w^{\alpha_1} (1 - w)^{\alpha_2}$, with α_1 and α_2 characterizing the sharpness of the P Cygni profile. We first applied a P Cygni model to replace the Fe XXVI Ly α emission and absorption lines. We fixed the parameters γ and w_0 to 2 and 0.001, respectively (note that these parameters do not have any strong influence on the shape of the profile; by trying different values, we found that they are suitable for the fits on both CN and XN observations). We thus let five parameters free to vary during the fit: the characteristic energy of the profile E_0 (corresponding to the beginning of the absorption feature), the terminal velocity v_∞ , and the parameters τ_{tot} , α_1 , and α_2 . We then added another P Cygni model in order to fit the second UFO. We chose the same free parameters, but we tied the

Table 5
Fits Performed above 3 keV with Two P Cygni Profiles

Parameters		Obs. CN	Obs. XN
P Cygni 1&2	E_0 (keV)	$6.32^{+0.05}_{-0.05}$	$6.35^{+0.04}_{-0.04}$
P Cygni 1	v_∞/c	$-0.32^{+0.012}_{-0.027}$	$-0.32^{+0.049}_{-0.012}$
	τ_{tot}	$0.17^{+0.02}_{-0.03}$	$0.13^{+0.001}_{-0.016}$
	α_1	$0.93^{+1.33}_{-0.84}$	$3.60^{+1.38}_{-0.37}$
	α_2	$0.17^{+0.77}_{-0.42}$	$1.58^{+0.91}_{-0.91}$
C or χ^2/dof		389.6/361 = 1.08	1187.5/1182 = 1.005
P Cygni 2	v_∞/c	$-0.52^{+0.024}_{-0.015}$	$-0.53^{+0.034}_{-0.022}$
	τ_{tot}	$0.04^{+0.004}_{-0.004}$	$0.02^{+0.003}_{-0.003}$
	α_1	$6.17^{+3.28}_{-7.18}$	$4.13^{+1.87}_{-3.22}$
	α_2	$-0.42^{+0.68}_{-0.63}$	$-0.68^{+0.22}_{-0.17}$
C or χ^2/dof		375.4/357 = 1.05	1170.3/1178 = 0.99
ΔC or $\Delta\chi^2/\Delta\text{dof}$		14.2/4	17.2/4

energy E_0 of the second P Cygni profile to that of the first P Cygni profile because a single Fe XXVI Ly α emission line was assumed for both UFOs (as also assumed in Section 3.3 and in the analysis from Reeves et al. 2018a, 2018b). This fit with the second UFO was thus made with nine free parameters. We performed the fits on observations CN and XN, and we show the results in Table 5.

The statistics of the fits (last line of Table 5) as well as the residuals (plotted in Figure 5) show that the use of a second P Cygni profile significantly improves the fit in both observations CN (at about 99% confidence level) and XN (at more than 99%

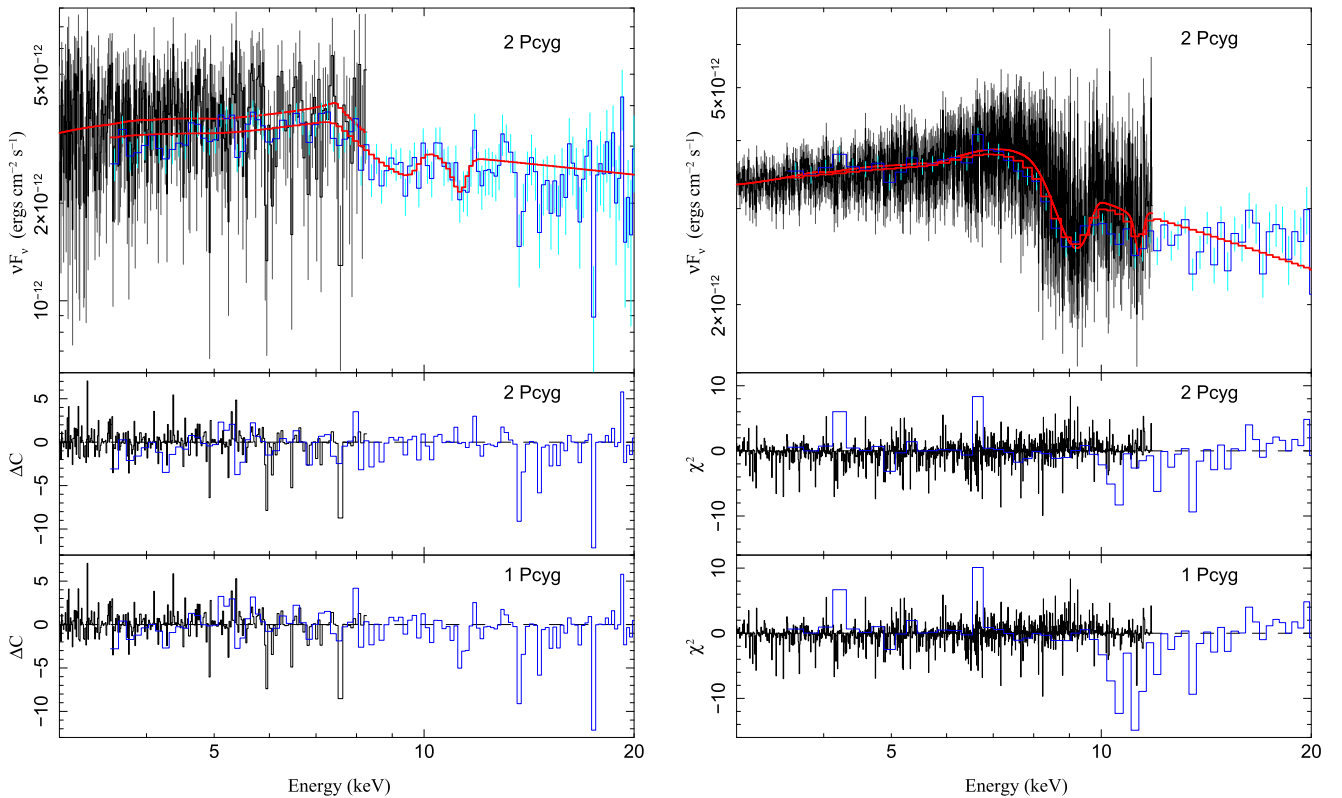


Figure 5. Unfolded hard spectra and residuals of observations CN (left) and XN (right) fit above 3 keV with two (top and middle) or one (bottom) P Cygni profiles (corresponding to two UFOs or one UFO, as described in Section 3.4). We especially note the improvement on the residuals above 10 keV when the second UFO is taken into account.

confidence level). This supports the hypothesis that a second UFO with a higher velocity than the first one is present in both data sets.

3.5. Photoionization Modeling

After our line identification at high energy (above 3 keV), we added the soft parts of the data (down to 0.4 keV) to our analysis and studied the broad energy band spectra. We initially performed a blind line search and identified individual lines, as described in the Appendix. Together with Sections 3.3 and 3.4, which focused on individual high-energy features, this blind line search aimed at detecting individual lines as signatures of the outflows, particularly at lower energy. Our analysis strategy is to study both individual lines (model-independent analysis) and global models (model-dependent analysis) in order to check the consistency of our results using a dual approach. For this purpose, we implemented a self-consistent photoionization modeling to reproduce the emission and absorption features seen in our broadband spectra of the three data sets CN, XN (from 0.4 to 30 keV), and C (from 0.4 to 8 keV). To do so, we used the XSTAR photoionization code (version 2.39, Kallman et al. 1996, 2004, 2009; Kallman & Bautista 2001). However, instead of using XSTAR tabulated grids for our fits (as has been done in previous works, e.g., Nardini et al. 2015; Matzeu et al. 2017a; Reeves et al. 2018a, 2018b), we employed the analytic XSTAR model *warmabs* to reproduce the absorption lines and *photemis* to generate the emission lines. Using these analytic functions requires a larger amount of computation time in comparison to the calculation of XSTAR tabulated grids. However, it allows us to explore the entire range of

values for the column density N_{H} , and the ionization parameter $\xi = L_{\text{ion}}/(nr^2)$ (with L_{ion} the ionizing luminosity, n the hydrogen density, and r the distance to the ionizing source), instead of discrete values that depend on the refinement of the grid. Furthermore, multiple parameters can freely vary during the fitting procedure, including the turbulent velocity.

Similarly to previous works (Matzeu et al. 2016b; Reeves et al. 2018b), we adopted two SEDs that are identical in the UV band. This assumption of an unchanged UV spectrum is supported by recent results from Reeves et al. (2018a). For observation XN, we used the SED reported in Nardini et al. (2015), derived from *XMM-Newton* EPIC-*pn* and *OM*, and from *NuSTAR*. For observations CN and C, we used an SED that slightly differs from the former only for the X-ray slope ($\Gamma = 2.3$ instead of 2.4, as found when fitting the continuum for CN data).

For our photoionization modeling, we added different wind emission and absorption components to the continuum of the three data sets, following the sequence described below and the order shown in the Table 6, which summarizes the results. We first replaced the partial covering wind *zpcfabs* with a *warmabs* model convolved with a *partcov* model (to account for the partial covering absorption required in all observations). To find the best fit, this partial covering absorber was variable in ionization, column density, covering factor, and velocity. Note that the outflowing velocities of the winds modeled with *warmabs* are derived from the redshift parameters, which were variable in the fitting process. We then included a photoemission component in this baseline model, having variable ionization, normalization, and velocity parameters, because emission lines such as the slightly

Table 6
Photoionization Models Applied to Our Data above 0.4 keV, and Corresponding Fit Parameters for Observations CN, XN, and C

Observation	Model				
		Parameters	“CN”	“XN”	“C”
CN	cst*tbabs*warmabs[ufo1]*warmabs[ufo2]*(photemis+partcov*warmabs[pc]*powerlaw+zgauss)				
XN	cst*tbabs*warmabs[wa]*warmabs[ufo1]*warmabs[ufo2]*(photemis+partcov*warmabs[pc]*powerlaw+zgauss)				
C	cst*tbabs*warmabs[ufo1]*(photemis+partcov*warmabs[pc]*powerlaw+zgauss)				
		Parameters	“CN”	“XN”	“C”
Cross-calibration		C	0.90 ^{+0.014} ₋₀	0.98 ^{+0.006} _{-0.007}	...
Galactic absorption		$N_{\text{H}}^{\text{gal}}$ (10^{22} cm ⁻²)	0.24 (f)	(f)	(f)
Power law		Γ	2.21 ^{+0.012} _{-0.008}	2.37 ^{+0.003} _{-0.003}	2.5 ^{+0.001} _{-0.004}
		$F_{0.4-30}$ keV (10^{-12} erg s ⁻¹ cm ⁻²)	11.30 ^{+0.10} _{-0.10}	15.33 ^{+0.018} _{-0.018}	17.10 ^{+0.17} _{-0.17}
Soft excess		E (keV)	0.40 ^{+0.07} _{-0.02}	0.55 ^{+0.008} _{-0.007}	0.087 ^{+0.041} _{-0.010}
		σ (keV)	0.05 ^{+0.008} _{-0.014}	0.24 ^{+0.003} _{-0.003}	0.057 ^{+0.0007} _{-0.0002}
		$F_{0.4-30}$ keV (10^{-12} erg s ⁻¹ cm ⁻²)	62.9 ^{+13.8} _{-15.8}	2.27 ^{+0.011} _{-0.011}	9.14 ^{+2.98} _{-3.60}
Partial covering		$\log(N_{\text{H}}/10^{22}$ cm ⁻²)	0.52 ^{+0.12} _{-0.13}	1.22 ^{+0.01} _{-0.04}	0.83 ^{+0.13} _{-0.08}
		$\log(\xi/\text{erg cm s}^{-1})$	3.20 ^{+0.18} _{-0.58}	3.04 ^{+0.02} _{-0.21}	2.89 ^{+0.08} _{-0.68}
		c_f	0.33 ^{+0.046} _{-0.054}	0.40 ^{+0.001} _{-0.003}	0.77 ^{+0.03} _{-0.04}
		v_{turb} (km s ⁻¹)	20000 (f)	(f)	(f)
		v_{out} (c)	-0.289 ^{+0.025} _{-0.030}	-0.268 ^{+0.007} _{-0.004}	-0.236 ^{+0.025} _{-0.064}
Wind emission		$\log(\xi/\text{erg cm s}^{-1})$	6.03 ^{+0.49} _{-0.28}	6.97 ^{+0.20} _{-0.51}	5.19 ^{+0.36} _{-0.09}
		norm ($\times 10^{-2}$)	8.5 ^{+5.2} _{-4.2}	5.8 ^{+0.1} _{-2.2}	5.3 ^{+0.092} _{-0.028}
		v_{turb} (km s ⁻¹)	20000 (f)	(f)	(f)
		v_{out} (c)	-0.056 ^{+0.006} _{-0.042}	-0.089 ^{+0.020} _{-0.001}	-0.026 ^{+0.002} _{-0.021}
		ΔC or $\Delta\chi^2/\Delta\text{dof}$	6.1/3	68.1/3	4.8/3
Warm absorption		$\log(N_{\text{H}}/10^{22}$ cm ⁻²)	...	-0.99 ^{+0.009} _{-0.002}	...
		$\log(\xi/\text{erg cm s}^{-1})$...	0.73 ^{+0.05} _{-0.21}	...
		v_{turb} (km s ⁻¹)	...	100 (f)	...
		v_{out} (c)	...	0 (f)	...
		$\Delta\chi^2/\Delta\text{dof}$...	74.5/2	...
Wind absorption 1		$\log(N_{\text{H}}/10^{22}$ cm ⁻²)	1.32 ^{+0.39} _{-0.22}	1.90 ^{+0.05} _{-0.46}	0.99 ^{+0.12} _{-0.24}
		$\log(\xi/\text{erg cm s}^{-1})$	6.03 ^{+0.49} _{-0.28} (t)	6.97 ^{+0.20} _{-0.51} (t)	5.19 ^{+0.36} _{-0.09} (t)
		v_{turb} (km s ⁻¹)	20000 (f)	(f)	(f)
		v_{out} (c)	-0.289 ^{+0.025} _{-0.030} (t)	-0.268 ^{+0.007} _{-0.004} (t)	-0.236 ^{+0.025} _{-0.064} (t)
		C or χ^2/dof	1660.2/1603 = 1.04	1860.7/1696 = 1.10	1384.2/1325 = 1.04
		ΔC or $\Delta\chi^2/\Delta\text{dof}$	21.4/1	406.0/1	19.4/1
Wind absorption 2		$\log(N_{\text{H}}/10^{22}$ cm ⁻²)	1.13 ^{+0.21} _{-1.31}	1.71 ^{+0.09} _{-0.58}	...
		$\log(\xi/\text{erg cm s}^{-1})$	6.03 ^{+0.49} _{-0.28} (t)	6.97 ^{+0.20} _{-0.51} (t)	...
		v_{turb} (km s ⁻¹)	20000 (f)	(f)	...
		v_{out} (c)	-0.478 ^{+0.031} _{-0.094}	-0.483 ^{+0.001} _{-0.033}	...
		C or χ^2/dof	1652.2/1601 = 1.03	1811.3/1694 = 1.07	...
		ΔC or $\Delta\chi^2/\Delta\text{dof}$	8.0/2	49.4/2	...

Note. (f) refers to parameters that have been frozen during the fits. (t) refers to parameters that have been tied to other parameters during the fits (such as the ionization parameters, and the velocities of the partially covering absorber and the slowest UFO). Each ΔC or $\Delta\chi^2$ value refers to the improvement of the fit when the new component is added to the model including the components listed above in the table.

blueshifted Fe XXVI Ly α have been detected, as described in the previous sections. We used free Doppler-shift parameters for both these models, allowing the emission and absorption features to be blueshifted independently. As seen in the statistics of the best-fit wind emission (ΔC and $\Delta\chi^2$ in Table 6), the wind emission is significantly required by XN data and is marginally needed by CN and C data. A low-ionization warm absorber at the systematic Doppler shift is also required by XN data alone, as shown by the significant improvement of the fit when this new component is included in the previous model (see $\Delta\chi^2$ value for the warm absorption in Table 6). We then applied a totally covering absorption to the

model described above (including the new continuum, the wind emission, and the warm absorber for the XN observation alone), with a variable column density, linking the ionization parameter to that of the photoemission, and linking the blueshift to the partial covering absorption, so we assumed that the partially covering absorber and the fast wind are outflowing at the same velocity, but are independent in ionization parameters and column densities. Adding this first UFO strongly improves the fit for all observations, with $\Delta C = 21.4$ for CN, $\Delta\chi^2 = 406.0$ for XN, and $\Delta C = 19.4$ for C, for one degree of freedom, demonstrating that the slowest UFO is significantly required in all our data sets at a confidence

level higher than 99.9%. We then included a second total covering absorption in the model with the first UFO, with a varying column density and an independent blueshift (i.e., an independent velocity), and an ionization fixed to the value of the first UFO and the emission component. We see that the inclusion of this higher-velocity UFO in the model improves the fit for observations CN and XN (see Table 6), with $\Delta C = 8.0$ for CN and $\Delta\chi^2 = 49.4$ for XN, for two degrees of freedom, showing that the fastest UFO is significantly required at confidence levels of >95% and >99.9%, respectively.

For these fits, we allowed the continuum parameters (power law, soft excess, and cross-calibration factor) to vary because the application of the `warmabs` models slightly changed the overall shape of the broadband spectra. Initially, we varied the turbulent velocity of each XSTAR component. We found that the turbulent velocity reached $20,000 \text{ km s}^{-1}$ for all components in all observations, so we fixed this parameter to this value. This high turbulent velocity is consistent with the large widths of the lines described in the previous sections, and with the values used in previous works with XSTAR grids. All abundances were fixed to solar values.

The fits were performed in ISIS using Cash statistics and the `powell` method for observations CN and C, and χ^2 statistics and the `mpfit` method for observation XN. Using the XSTARDB⁴ library of ISIS S-lang scripts, we list the strongest features predicted by our photoionization models with the fit parameters given in Table 6 for the three observations and for all components. For the UFOs, in addition to the expected Fe XXV He α , He β , Fe XXVI Ly α , and Ly β absorption lines, the XSTAR model predicts Si XIV and S XVI Ly α absorption lines at lower energy, consistent with the lines identified in the blind line search section (see appendix). Many emission features are also predicted by the `photemis` model, from Fe XXV He α and Fe XXVI Ly α , but also from other ions (C VI, O VIII, Ne X, Mg XII, Fe XXIV, Si XIV, and S XVI). The lower-ionization partially covering absorber is expected to show absorption features from O VII, O VIII, Fe XVII, Fe XVIII, Ne IX, Ne X, Mg XI, and Si XIII ions. Some of these lines have also been identified in the blind line search section. Non-blueshifted signatures from O VII and Ne VI ions are predicted for the warm absorber found in the XN observation. We also used a Markov chain Monte Carlo (MCMC) approach to derive the probability distribution of each parameter via Bayesian data analysis. For this purpose, we used the `isis_emcee_hammer` function⁵ developed in ISIS S-lang by MN. Best-fit values and error bars are reported in Table 6. Figure 6 shows the contour plots characterizing the absorbers in the three observations.

4. Discussion

4.1. Modeling the Highly Ionized Features

We initially modeled the absorption features at high energy (above 3 keV) with blueshifted and highly ionized iron lines to characterize the UFOs in PDS 456. We found that the Fe XXV Ly α emission and absorption lines, the Fe XXVI Ly β absorption line, and the Fe K edge corresponding to the fit with only one UFO are significantly or marginally detected in both observations CN and XN. Velocities in emission and in absorption derived from this fit are consistent with results from

Nardini et al. (2015; see Table 3). Applying a second set of lines to account for the second possible UFO marginally improved the fit, but not all the lines were detected significantly (see Table 4). This can be explained by the complexity of the model fit to data with an insufficient resolution. Indeed, signatures of the second UFO are located in the energy band that are predominantly covered by *NuSTAR*. However, the second UFO is required, more convincingly in observation XN than in observation CN, according to the residuals in Figure 4.

We replaced the sets of Gaussian lines with P Cygni profiles using the model from Done et al. (2007), as proposed by Hagino et al. (2015) and Nardini et al. (2015), describing a spherically symmetric outflowing wind. Applying two P Cygni models instead of a single model significantly improved the fits for both observation CN and XN (see the statistics in Table 5 and the residuals in Figure 5). Table 5 shows that the velocities implied by the P Cygni model are slightly higher (by about 15%–20%) than the velocity measured from individual Gaussian lines. The terminal velocity of the wind, v_∞ , is a characteristic parameter of the P Cygni model for a quasi-spherical fully covering outflow. This value is the actual speed of the outflowing gas. However, v_∞ strongly depends on the P Cygni model used to fit our data, so we instead considered the line-of-sight bulk velocity, which is found to have consistent values when fitting with Gaussian lines and photoionization models, for our analysis and for energetic estimations. We found an optical depth for the first P Cygni profile that is consistent with results from Nardini et al. (2015), the depth of the second P Cygni profile being lower. Parameters α_1 and α_2 are different from values found by Nardini et al. (2015), possibly because they were free to vary independently in our analysis. Their values are also very different between the observations, as well as between the two P Cygni profiles.

For both observations CN and XN, the outflow velocities of both UFOs measured by one method or the other one are consistent between the two different epochs and are also consistent with previous results (e.g., Nardini et al. 2015; Matzeu et al. 2017a; Reeves et al. 2018b).

4.2. Photoionization Results

We applied self-consistent XSTAR photoionization models to our three different epochs of observations (using the entire detector band, i.e., 0.4–30 keV when possible) in order to characterize the physical properties of the absorbers reproducing different absorption lines detected in our blind line search (see Appendix) and in high-energy spectra (see Sections 3.3 and 3.4). The statistics of the fits (ΔC and $\Delta\chi^2$ rows in Table 6) demonstrate that including the two UFO components in our modeling significantly improves the fits (at >99.9% confidence level for the slowest UFO, and at > 95 to >99.9% confidence level for the fastest UFO). The high values of column densities N_H and ionization parameters ξ obtained from our modeling are typical of UFOs (e.g., Tombesi et al. 2013) and consistent with previous studies of PDS 456.

As described in Section 3.5, we adopted a fixed value for the turbulent velocity, which helped to constrain the other parameters better because the model is complex with many free parameters. The turbulent velocity of $20,000 \text{ km s}^{-1}$ is consistent with the large widths of individual lines (e.g., see Table 7), and the values reported in previous studies (e.g., Nardini et al. 2015).

The ionization parameter of both UFOs was tied to that of the emission associated with the disk wind to facilitate the fits,

⁴ <http://space.mit.edu/cxc/analysis/xstarbd/index.html>

⁵ <https://www.sternwarte.uni-erlangen.de/wiki/index.php/Emcee>

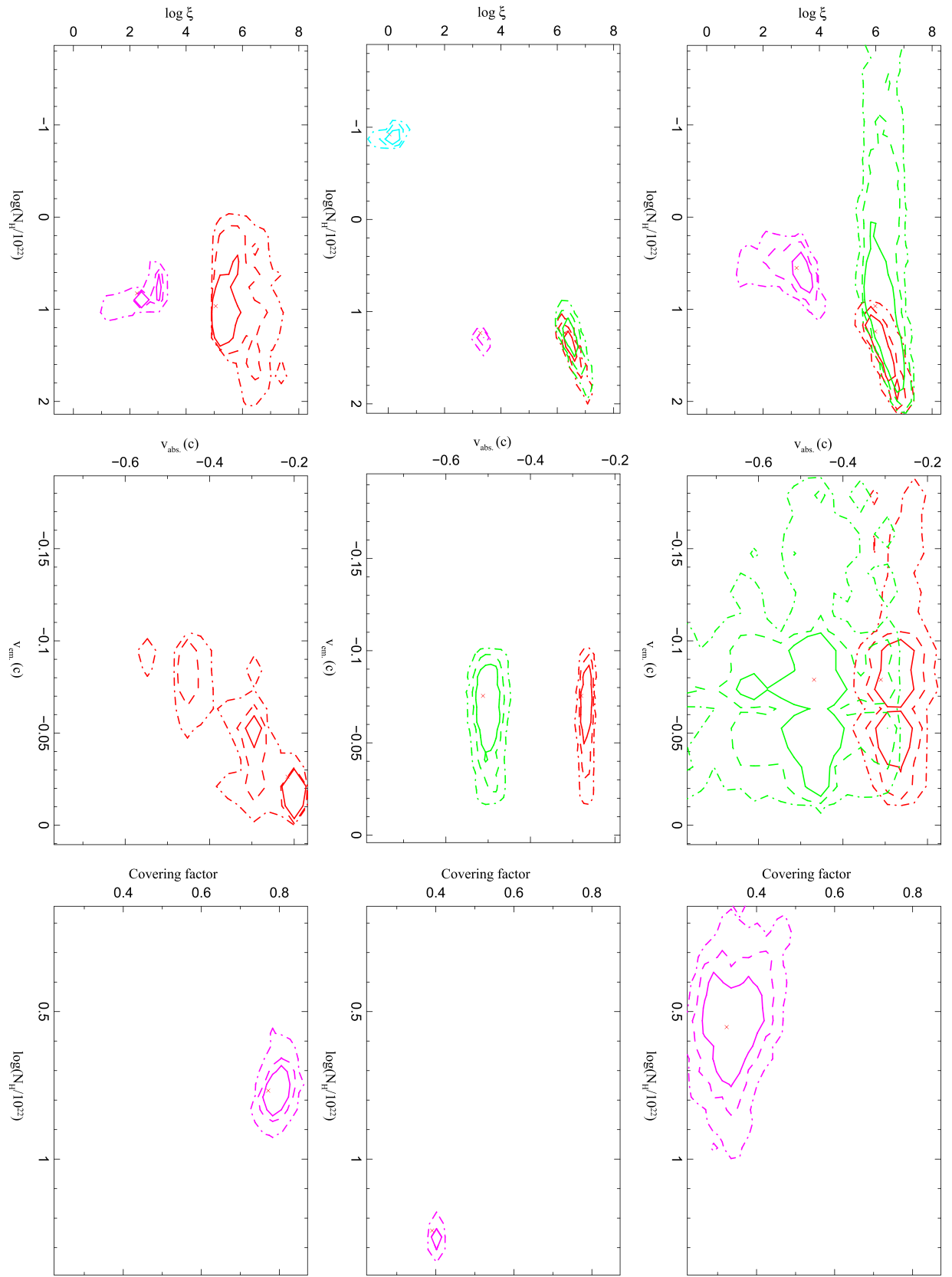


Figure 6. Parameter contours from the absorbers in the three observations (results of the photoionization modeling performed above 0.4 keV). Left: ionization parameter vs. column density. Middle: velocity in absorption vs. velocity in emission. Right: covering factor vs. column density of the partial covering absorber. Top: observation CN. Middle: observation XN. Bottom: observation C. Three confidence levels are represented and are shown with a solid line for 68%, a dashed line for 90%, and a dot-dashed line for 99%. Like in previous figures, pink contours represent parameters from the partially covering absorber, red contours are for the slowest UFO, green contours are for the fastest UFO, and light blue contours are from the low-ionization warm absorber detected in observation XN.

as implemented in Nardini et al. (2015) and Reeves et al. (2018b), so the ionization parameters of both UFO are the same, but different from the ionization parameter of the partial covering absorber (even if the partially covering absorber has the same velocity as the slowest UFO). The high-ionization parameters derived from our modeling are consistent with the detection of highly ionized Fe XXVI lines and similar to previous results (e.g., Nardini et al. 2015; Reeves et al. 2018a, 2018b). It is also possible that two different sets of emission and absorption from different stratification layers of a single UFO are associated with the different ionizations. However, the available data would not be able to distinguish the different kinematic components, the overall model being in this case even more complex.

The velocity of the slowest UFO was tied to the velocity of the partially covering absorber. This scenario was adopted to obtain a better constraint. However, we saw in the appendix that when we identified lines that were detected by blind search, the transitions had a slightly different blueshift for lines from the partially covering absorber than from the slowest UFO, in particular in observation CN. It may imply that the actual velocities of both components are slightly different. The high UFO velocities derived from photoionization modeling (about $v_{\text{out}} = -0.24$ to $-0.29 c$ for the slowest UFO, and $v_{\text{out}} = -0.48 c$ for the fastest UFO) are consistent with previous studies, as well as with results from modeling of high-energy features (see Sections 3.3 and 3.4) and results from the blind line search (see the Appendix). An additional method for the characterization of the kinematic components of the UFOs is also described and applied to PDS 456 data in the Appendix, and the results are also consistent with values found through photoionization modeling.

The MCMC approach gave us the probability distribution of each parameter of the photoionization model, giving contours shown in Figure 6. These contour plots show the behavior of the ionization parameter as a function of the column density, as well as the different velocities in emission and in absorption, for all absorbers detected in the three observations, and the variation of the covering factor as a function of the column density for the partially covering absorber in the three observations. We find that the velocities are consistent between observations CN and XN, with a better constraint for observation XN than for observation CN because of the better signal-to-noise ratio. Despite the poor constraint on the velocity of the UFO detected in observation C (corresponding to the slowest one), we can see hints of a consistency with the other observations, with the best-fit value slightly higher than $v_{\text{out}} = -0.2 c$ and contours coherent with an outflowing velocity of $v_{\text{out}} = -0.2$ to $-0.3 c$. Contours of the UFO in observation C are obviously improved when *NuSTAR* data are combined with *Chandra*/HETGS data, as in observation CN. However, despite the lack of information at high energy in observation C, the photoionization modeling allowed us to constrain the parameters of the winds at a lower significance level. The contours of all parameters, and in particular, the parameters of the fastest UFO, are more precise for observation XN than for observation CN (regarding velocities, ionization parameters, column densities, and covering factors), as expected because the signal-to-noise ratio in the *NuSTAR* energy band that we achieved by combining all observations XN1 to XN5 is higher than that from observation CN. The ionization parameters and column densities of the UFOs are relatively stable between the different epochs. The

ionization of the partially covering absorber is lower than those of the UFOs, as expected from the detected absorption lines in the soft band, and this parameter is stable between observations, with a modest value ($\log(\xi) \sim 3$) that is consistent with previous studies (Nardini et al. 2015; Reeves et al. 2018a). The variability of the covering factor ($c_f \sim 0.3$ – 0.8) and of the column density of this absorber ($N_{\text{H}} = (3.3$ – $16.6) \times 10^{22} \text{ cm}^{-2}$), as seen in the right panel of Figure 6, could be responsible for the continuum shape variability observed in all observations of PDS 456, similar to NGC 5548 (Kaastra et al. 2014; Nardini et al. 2015; Reeves et al. 2018a).

An alternative scenario proposed to explain blueshifted absorption features is that they could be the signatures of reflection on an optically thick plasma that may cover the accretion disk whose inner parts may rotate at extremely high velocities, producing a relativistic blueshifted Fe K-shell feature (see the example of PG 1211+143, Gallo & Fabian 2013, but also the counterargument from Lobban et al. 2016). Nardini et al. (2015) found that such a reflection-dominated scenario underpredicts the strength of the absorption feature by about 9 keV. Behar et al. (2010) found a persistent but small contribution of a reflection component in most observations before the *XMM-Newton* observation in 2007. A *Suzaku* observation from 2007 shows a marginally significant hard X-ray excess that could be modeled either by a strong reflection component or by a Compton-thick partially covering absorber (Reeves et al. 2009). Reprocessed and scattered X-ray emission off the surface of an accretion disk wind could explain the low flux and hard X-ray spectrum of the *Suzaku* observation from 2011, but this scenario is only applicable for this particular state (Reeves et al. 2014). There is no sign of dominating reflection in the spectra of observations CN and XN. Because adding a reflection component to the continuum did not significantly improve the fit (see Section 3.2), we tried to consider neutral reflection in our photoionization modeling (using `pexmon`) because the ionized absorbers provide a better constraint on the complicated spectral shape around 9 keV than the continuum model. However, adding this `pexmon` reflection component to the photoionization model with the two UFOs did not improve the fits ($\Delta C = 1.66$ for observation CN and $\Delta\chi^2 = -12.3$ for observation XN for three parameters of interest). Furthermore, the parameters of this reflection component, i.e., the reflection factor, the abundance, and the inclination, were poorly constrained during the fits for both observations, even through the MCMC approach.

4.3. Thermal Stability

To investigate the effects of the continuum on the ionization balance and thermal stability of the photoionized gas, we produced thermal stability curves, plotting the temperature of the plasma $\log(T)$ as a function of $\log(\xi/T)$ (Krolik et al. 1981; Reynolds & Fabian 1995; Krolik & Kriss 2001; Chakravorty et al. 2009; Lee et al. 2013). These curves represent the thermal equilibrium of the gas. On one side of the curve, cooling dominates, while on the other side, at high ionization and low temperature, heating dominates. Generally, a positive gradient of the curve indicates thermal stability for the gas (indeed, a small increase in temperature will increase the cooling, while a perturbation decreasing the temperature will increase the heating). Conversely, a negative gradient is present in regions of instability. We used the two SEDs described in Section 3.5 to produce the thermal stability curves shown in Figure 7. We

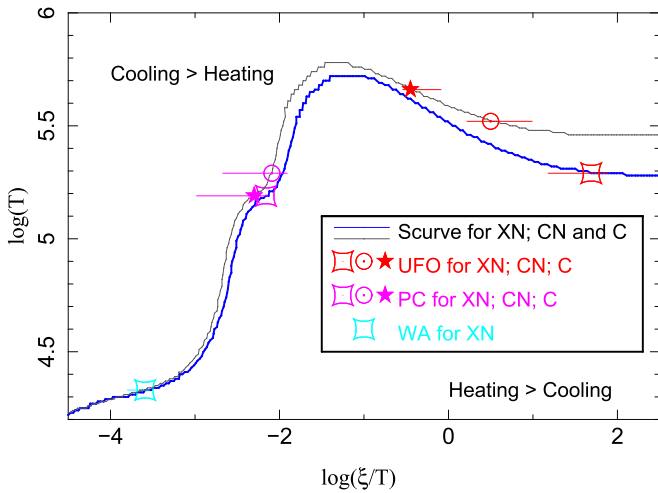


Figure 7. Thermal stability curve for the photoionized gas in PDS 456, calculated for the SED described by Nardini et al. (2015) for observation XN (dark blue line) and for the slightly modified SED for observations CN and C (gray line). It shows the distribution of equilibrium temperature $\log(T)$ as a function of $\log(\xi/T)$. The position of the absorbers detected in the three observations are overplotted, according to their ξ values and error bars at the 68% confidence level resulting from the MCMC routine. Red points represent the ionization of the photoemission and the UFOs, pink is used for the ionization of the partial covering (PC) absorber, and light blue represents the ionization of the warm absorber (WA) of observation XN.

recall here that these two SEDs are identical in the UV band and slightly differ in X-rays in order to match our three data sets. Note that the stability curve depends on the input assumptions provided to the photoionization code. Its shape is influenced by the ionizing SED (e.g., Lee et al. 2013; Mehdipour et al. 2015) and by the density and chemical composition of the absorber (e.g., Chakravorty et al. 2009). The unusual decrease in temperature at high ionization can be explained by the fact that the SED we used for the calculation of the XSTAR models has a strong soft component (as shown in Figure 5 from Matzeu et al. 2016b), and as the Compton temperature ($T_{IC} = \langle E \rangle / 4k$) depends on the mean energy photon, the value of the Compton temperature is low. When the gas is fully ionized, it reaches this Compton temperature (Kallman & Bautista 2001). However, when the gas is partially ionized, it can reach hotter temperatures, explaining the peak shown in Figure 7. Indeed, in addition to the heating of the gas from the energetic electrons produced by photoionization, these electrons can heat the gas to a higher temperature through secondary collisional ionization of neutral atoms.

We overplotted points representing the absorbers, whose ionization parameters have been characterized by the photoionization models in the three observations, on top of their respective stability curves. We can see that the partial covering absorber is in a stable state in all observations (pink points), in the portion of the curve with a positive slope. This is also the case for the non-blueshifted warm absorber (light blue rectangle) detected in observation XN. However, because the UFO components of observations XN, CN, and C are on a negative gradient branch (red points), we might expect that this gas is thermally unstable. However, the cooling time for the UFO gas is much shorter than the outflow time (R/v_{out}), so the gas should be stable in order for the UFO to be persistent and observable. In fact, the thermal stability of the gas can be determined by the slope of the branches, as described above,

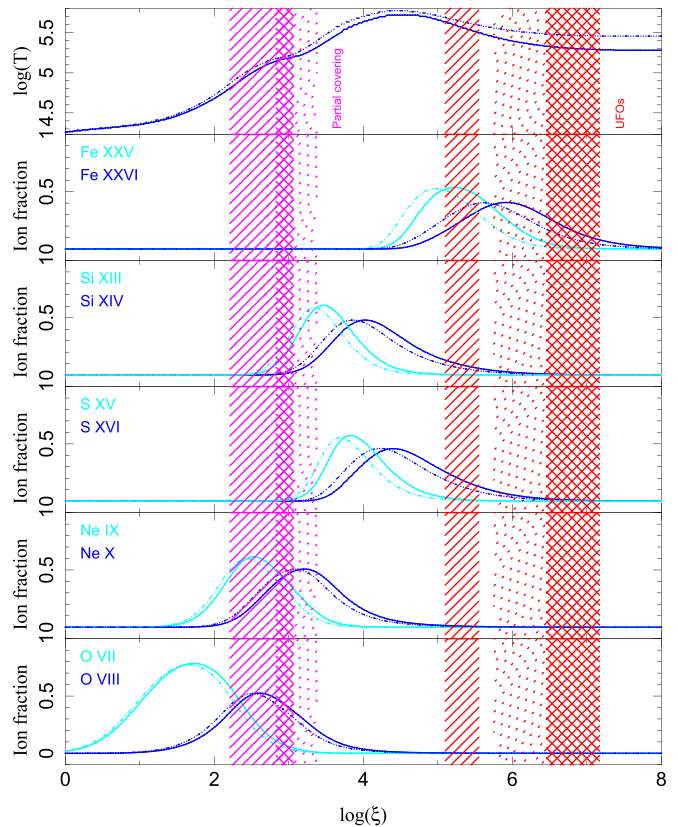


Figure 8. Distribution of the temperature and of the ion fractions of elements that have been identified in our three data sets as a function of the ionization parameter. Solid lines corresponds to the SED used by XSTAR for the XN observation, while dashed lines represent the SED used for the CN and C observations. The partially covering absorbers are identified in pink, while UFOs are represented in red (CN: dotted zone, XN: checkered zone, and C: hatched zone).

only in the case of S shapes. However, for our case, the thermal stability curve, with its unusual negative slope at high ionization, does not follow this rule. Indeed, as shown in Figure 7, at high ionization, cooling dominates above the curve and heating dominates below the curve. On this high-ionization branch, a small perturbation that increases the temperature will therefore bring the gas to a region where cooling dominates, and a small decrease in temperature will increase the heating. The UFOs located on this branch at high ionization are thus stable after all.

Figure 8 shows the distribution of the temperature as a function of the ionization parameter, as well as the distribution of ion fractions of the H-like and He-like ions of the elements identified in the three data sets, as described in previous sections (Fe, Si, S, Ne, and O). This distribution is dependent on the SED used by the photoionization code XSTAR, as we can see in the difference between solid and dashed lines (see the legend of the figure for more details). We overplot the values of the ionization parameters obtained by photoionization modeling, for both partial covering absorbers (in pink) and UFOs (in red), in the three observations (CN: dotted zone, XN: checkered zone, and C: hatched zone). We can see that the ions of Ne and O detected in the three observations can coexist in a single ionization zone at the same velocity, originating from the partial covering absorbers (pink zone). Iron ions are also detected in the three data sets, and can coexist with S and Si ions in a single ionization zone corresponding to the UFOs (red

zone). This coexistence is more significant in observation C than in observations XN and CN. S and Si ions could either be produced by the UFOs or by the partially covering absorbers. This uncertain origin is induced by the fact that to simplify the model applied to our data, we linked the velocities of the partially covering absorber and of the slowest UFO together, as well as the ionization parameters between both UFOs. Higher-quality data are required to allow the modeling with untied parameters and hence the precise determination of the origin of the detected S and Si ions. In the present study, despite their dependence on the assumptions made for the fitting, the distributions of ion fractions of different elements show that their coexistence is possible, giving indications of their origins, and thus support the results from the photoionization modeling, as well as the identification of the lines detected by the blind line search.

4.4. Comparison of Results from Different Epochs

We found that two UFOs are significantly detected in our observations CN and XN, the detection being even more convincing in observation XN. The velocity of the slowest UFO obtained by photoionization modeling on observation XN ($v_{\text{out1}} = -0.268_{-0.004}^{+0.007}c$) is consistent with the average value measured on the five individual XN1 to XN5 observations by Nardini et al. (2015) ($v_{\text{out1,average}} = -0.25_{-0.01}^{+0.01}c$).

The second UFO was not detected in the individual XN observations, as claimed by Reeves et al. (2018a, 2018b). Indeed, after finding a second, faster absorber in recent *XMM-Newton* and *NuSTAR* data from 2017, the authors reanalyzed the XN1 to XN5 observations, but did not find any signature of a second UFO above 10 keV. For our work, we chose to combine all the XN observations together, as explained in Section 3.1, as we wished to achieve the optimum signal-to-noise ratio using all available data. We verified the detection of the fastest UFO in the individual XN observations by applying the fitting procedure described in Section 3.3 on these five data sets, using two sets of Fe lines to look for signatures of both UFOs. Regarding the improvement of the fit statistics when considering two UFOs instead of one, and according to the significant detection of the Fe XXVI Ly α , Ly β , and K-edge features from the fastest UFO, we found that the second UFO is required by the data XN5 ($\Delta\chi^2/\Delta\text{dof} = 19.03/5$, >99.9% confidence level), XN2, ($\Delta\chi^2/\Delta\text{dof} = 15.82/5$, about 99.5% confidence level) and XN4 ($\Delta\chi^2/\Delta\text{dof} = 10.16/5$, >90% confidence level). However, we did not detect the second UFO in observations XN3 and XN1. Looking at their recent observations from 2017, Reeves et al. (2018b) detected the second UFO with a significance >99.9% (the addition of the Ly α line from the fastest UFO improving the fit by $\Delta\chi^2 = 39.3$ for two free parameters). The detection of the lines from the second UFO is less significant in XN5, XN2, and XN4 data than in the more recent data from 2017; this is probably why Reeves et al. (2018a, 2018b) considered that this fastest component was not visible in the individual XN observations. According to the count rate of each observation shown in Table 1 and to the lower flux of the recent data from 2017, there seems to be a hint of an anticorrelation between the statistical confidence level for the detection of the fastest UFO and the flux intensity of PDS 456. This trend is consistent with the proposition from Reeves et al. (2018a), who suggested that PDS 456 has to be in a low state to allow the detection of the second UFO (see further discussion in Section 4.5).

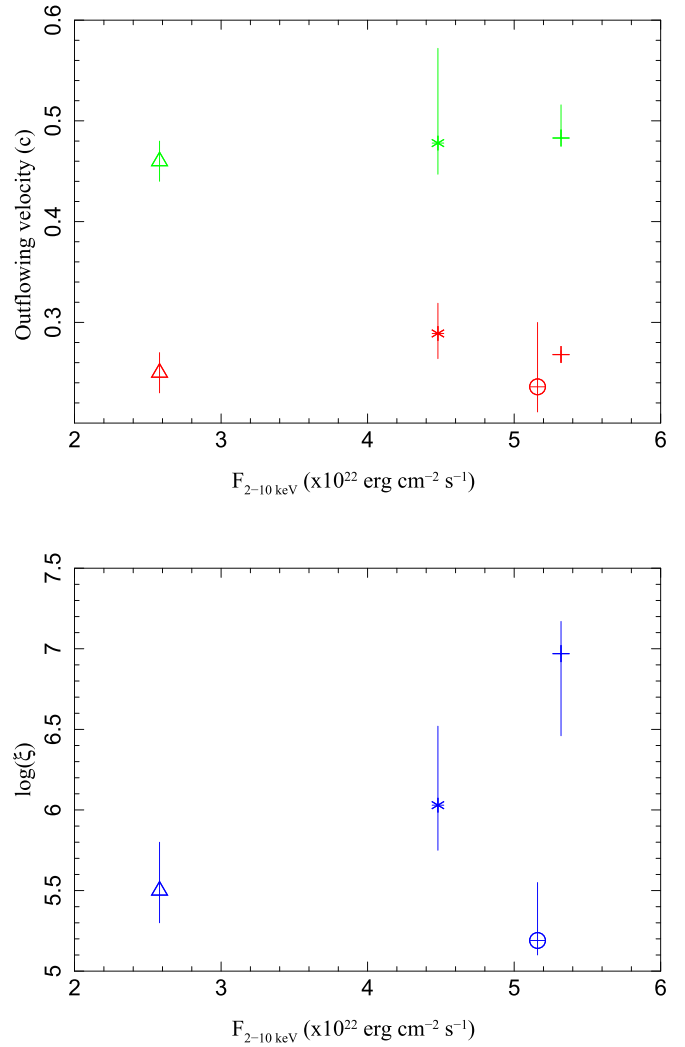


Figure 9. Top: outflow velocity as a function of the intrinsic flux between 2 and 10 keV. Red points represent the values for the slowest UFO, and green points are for the fastest UFO. Triangles represent results of Reeves et al. (2018b), the cross is used for our CN observation, the plus for observation XN, and circles for observation C. Bottom: ionization parameter of the UFOs resulting from photoionization modeling as a function of the intrinsic flux between 2 and 10 keV. The symbols used in the bottom panel are the same as in the top panel.

In our observations CN and XN, the column density of the fastest UFO is lower than the density of the slowest UFO (see Table 6), consistent with results from Reeves et al. (2018b).

Figure 9 shows the outflow velocities (top panel) and the ionization parameters (bottom panel) of the UFOs detected in our analysis and in the *XMM-Newton*/*NuSTAR* data from 2017 (Reeves et al. 2018b) as a function of the intrinsic flux of PDS 456 between 2 and 10 keV. We can see that the velocities are similar between the different observations. In the study of 12 previous X-ray observations of PDS 456, Matzeu et al. (2017a) depicted a strong correlation between the outflow velocity and the X-ray luminosity, which supports the hypothesis of a radiatively driven wind in PDS 456, boosted by line driving (Hagino et al. 2016). The recent detection of the C IV BAL at the velocity of 0.3 c in *HST* UV observations may also boost the opacities in UFOs for radiative driving (Hamann et al. 2018). This hypothesis of radiative driving is also strongly supported by the fact that the SMBH of PDS 456 is accreting at a regime near the Eddington limit (King & Pounds 2003;

Gofford et al. 2014; Matzeu et al. 2017a). We checked the correlation between velocity and luminosity of the data shown in Figure 9. We only found a possible small correlation between intrinsic flux and velocity of the fastest UFO (Pearson correlation coefficient $r = 0.995$, p -value = 0.06), and no correlation between the flux and the velocity of the slowest UFO ($r = 0.11$, p -value = 0.89). The outflowing velocities seem rather to have stable values. We only found a non-significant correlation for the expected positive relation between the ionizing flux and the ionization parameter ($r = 0.40$, p -value = 0.60), probably because of the less precise constraint on the slowest UFO with *Chandra* data from observation C compared to the parametric constraints derived from additional high-energy data available in observations CN and XN.

4.5. Wind Mass Outflow Rates and Energetics

The mass outflow rate is

$$\dot{M}_{\text{out}} \sim \Omega N_{\text{H}} m_p v_{\text{out}} R_{\text{in}}, \quad (3)$$

where Ω is the solid angle, N_{H} is the column density, m_p is the proton mass, v_{out} is the outflowing velocity, and R_{in} is the starting point of the wind (see details, e.g., in Nardini et al. 2015). We used an approximated value of $\Omega = 2\pi$ for the solid angle, as justified by Nardini et al. (2015; see their discussion in the supplementary material for further details, as well as the argumentation from Reeves et al. 2018a). The column density is directly derived from the photoionization modeling, as well as the outflow velocity (see Table 6). In the case of a radiatively accelerated wind (e.g., Matzeu et al. 2017a), R_{in} can be approximated as

$$R_{\text{in}} \sim 2 \left(\alpha \frac{L}{L_{\text{Edd}}} - 1 \right) \left(\frac{v_{\infty}}{c} \right)^{-2}, \quad (4)$$

where v_{∞} is the wind terminal velocity and α is a force multiplier factor (Reeves et al. 2018b). PDS 456 is accreting at about the Eddington limit, so we could approximate $L/L_{\text{Edd}} = 1$. Using a factor of $\alpha = 2$ (as done by Reeves et al. 2018b) and the outflow velocities derived from photoionization modeling for each of our three observations, we find that the launching radius is $\sim 5 \times 10^{15}$ cm (or $30R_g$ for $M_{\text{BH}} = 10^9 M_{\odot}$) for the slowest UFO and $\sim 1 \times 10^{15}$ cm (or $9R_g$) for the fastest UFO. These values are close to the escape radii $R_{\text{escape}} = \frac{2GM}{v_{\text{out}}^2}$, i.e., the minimum radii from which winds of a given outflow velocity can be launched. We are probably observing a stratified UFO in PDS 456, with several components from multiple stratification layers having different velocities and being launched from the accretion flow close to the SMBH (e.g., Tombesi et al. 2013; Reeves et al. 2018b). Reeves et al. (2018b) proposed that PDS 456 has to be in a low state for the source to not be extremely luminous (and the iron fully ionized), to allow the detection of the second UFO at such short distances. This trend seems to be verified considering the high confidence level of the detection of the second UFO in individual XN observations as a function of the flux, as explained in Section 4.4. An alternative explanation could be that a partially covering dense gas (as the one already observed in previous studies) is shielding the innermost wind, preventing

it from becoming too highly ionized (Matzeu et al. 2016a; Reeves et al. 2018b).

The maximum radial distance of the absorbers can be estimated by considering that $\Delta R/R < 1$, i.e., their thickness cannot exceed their distance from the ionizing source (e.g., Reeves et al. 2003, 2018b). With the definition of the ionization parameter given in Section 3.5, $R_{\text{max}} < L_{\text{ion}}/N_{\text{H}}\xi$. This gives maximum radii of 7×10^{17} cm (or $4700R_g$) for observation CN, 2×10^{16} cm (or $130R_g$) for observation XN, and 6×10^{18} cm (or $40,000R_g$) for observation C. Thus, the outflows in PDS 456 may extend to the broad line region.

For the slowest UFO, we found a mass outflow rate of $1.2 M_{\odot} \text{ yr}^{-1} = 0.05 \dot{M}_{\text{Edd}}$ for observation CN, $4.4 M_{\odot} \text{ yr}^{-1} = 0.2 \dot{M}_{\text{Edd}}$ for observation XN, and $0.6 M_{\odot} \text{ yr}^{-1} = 0.03 \dot{M}_{\text{Edd}}$ for observation C. For the fastest UFO, we found $0.4 M_{\odot} \text{ yr}^{-1} = 0.02 \dot{M}_{\text{Edd}}$ for observation CN, and $1.6 M_{\odot} \text{ yr}^{-1} = 0.07 \dot{M}_{\text{Edd}}$ for observation XN. We found a different value for the mass outflow rate of the slowest UFO for observation XN compared to previous studies (with, e.g., an estimated kinetic power and mass outflow rate of $\sim 15\%$ and $\sim 50\%$, respectively, of Eddington values for Nardini et al. 2015, and 5% and 40% for Gofford et al. 2014) because we obtained slightly different parameters resulting from the photoionization fit and because we used a lower value for the inner radius, calculated in the case of radiatively driven winds, while others used a timing approach to estimate it at a few hundred gravitational radii (Reeves et al. 2009; Nardini et al. 2015; Matzeu et al. 2016a, 2016b). We see that the mass outflow rate of the fastest UFO is lower than the rate from the slowest UFO. We calculated the kinetic power of the winds ($P_{\text{kin}} = 0.5 \dot{M} v_{\text{out}}^2$) and found kinetic powers of $0.02 L_{\text{Edd}}$ for observation CN, 0.07 – $0.08 L_{\text{Edd}}$ for observation XN, and $0.008 L_{\text{Edd}}$ for observation C (again slightly lower than in previous works for the same reason as above). Both winds are found to have a similar kinetic energy, which contradicts the prediction of a higher power for the faster UFO, as estimated by Reeves et al. (2018b) using the approximation that $P_{\text{kin}} \propto v_{\text{out}}^3$. The high velocities and high column density characterizing the UFOs detected in our three observations result in a large amount of kinetic power of about 0.8%–8% of the bolometric luminosity, which is sufficient to induce significant AGN feedback according to models of black hole and host galaxy coevolution (King & Pounds 2003; Di Matteo et al. 2005; Hopkins & Elvis 2010).

5. Conclusion

We presented the analysis of simultaneous *Chandra*/HETGS and *NuSTAR* observations of PDS 456 from 2015 (CN), simultaneous *XMM-Newton* and *NuSTAR* data from 2013 to 2014 (XN), and *Chandra*/HETGS data from 2003 (C). We performed a dual-approach study of these selected observations of the quasar, analyzing data from the three different epochs in a consistent way, using both model-independent and model-dependent techniques.

We confirmed the presence of the persistent UFO at a velocity of $v_{\text{out}} = -0.24$ to $-0.29 c$ that was observed in previous studies (e.g., Reeves et al. 2009; Nardini et al. 2015). We also detected a faster UFO ($v_{\text{out}} = -0.48 c$) in the CN and XN observations, which was previously only reported in very recent observations (Reeves et al. 2018a, 2018b). In the model-independent approach, we observed their signatures via deep absorption troughs at about 9 and 11 keV, corresponding to blueshifted, highly ionized iron K-shell transitions, which form P Cygni profiles when the associated blueshifted emission is

considered. We also identified other lines in the HETGS spectra that are blueshifted at the same extreme velocities at lower energies, e.g., Si XIV Ly α , S XVI Ly α , O VIII Ly α , Ne X Ly α , and possible contribution from nickel at high energy.

In the model-dependent approach, we performed photoionization modeling to characterize both UFOs ($\log(\xi) \sim (6-7) \text{ erg cm s}^{-1}$, $N_{\text{H}} \sim (1-8) \times 10^{23} \text{ cm}^{-2}$) as well as the partially covering absorber ($\log(\xi) \sim 3 \text{ erg cm s}^{-1}$, $N_{\text{H}} \sim 3 \times 10^{22-2} \times 10^{23} \text{ cm}^{-2}$, $c_f \sim 0.3-0.8$). We found that all the winds detected in the three data sets are thermally stable and can coexist.

The outflow of PDS 456 is probably composed of several components from multiple layers having different velocities and ionizations, launched from the accretion flow close to the SMBH, and certainly radiatively driven. Both relativistic components of the outflow are powerful enough to play a role in the evolution of the host galaxy, with mass outflow rates of 2%–20% and kinetic powers of 0.8%–8% of the Eddington values.

We performed an analysis using different methods that led to consistent results. However, we made some assumptions in order to be able to constrain the wind characteristics because of the complexity of the models we applied to our data. Further simultaneous and high signal-to-noise ratio data are required in order to test our assumptions. Future high-resolution instruments such as *ARCUS* and *Athena* will be useful to determine the structure of the high-velocity winds in PDS 456 more precisely.

We thank the anonymous referee very much for useful comments and corrections that helped to improve this paper. We gratefully acknowledge Claude Canizares for the *Chandra*/HETGS GTO time to observe PDS 456. We sincerely thank Tim Kallman for our private communication about stability curves for photoionized gas. R.B.M. acknowledge Emanuele Nardini and Chris Done for providing the P Cygni profile model used in this paper. We thank Fiona Harrison, PI of *NuSTAR*, for DDT time. Support for this work was provided in part by the National Aeronautics and Space Administration (NASA) through the Smithsonian Astrophysical Observatory (SAO) contract SV3-73016 to MIT for support of the *Chandra* X-Ray Center (CXC), which is operated by SAO for and on behalf of NASA under contract NAS8-03060.

Appendix A Blind Line Detection

We performed a blind line search in the broad energy band for observations CN and C, and the hard-energy band for observation XN. To perform this blind line search, we added 50 Gaussian lines to our continuum (described in Section 3.2) that we allowed to be either in emission or in absorption. We used the `gabs` models in order to take eventual saturation of the lines into account. We first fixed the continuum, added one Gaussian model (with free energy, width, and strength, i.e., three parameters of interest), fit the data, varied the continuum parameters, and again fit the data, and then fixed everything before running this sequence again for 50 iterations. We kept only statistically significant lines for which we obtained a ΔC or $\Delta\chi^2$ larger than 6.25, corresponding to 90% confidence level for three degrees of freedom. Note that these estimates of the line significance might be slightly overestimated, according to Protassov et al. (2002). The results of this blind line search

and line identification are presented in Table 7 and Figure 10 for observation CN, Table 8 and Figure 11 for observation XN, and Table 9 and Figure 12 for observation C. The tables give the rest energy of each line, together with its width, equivalent width, and significance. We tentatively identified some of the detected emission and absorption lines (reported in the tables), considering the transitions of the strongest lines resulting from the photoionization modeling described in Section 3.5. We also considered weaker contributions from higher-Z elements, such as the H-like transition of nickel. Even if Ni is 20 times less abundant than Fe (Grevesse & Sauval 1998), and thus negligible in XSTAR photoionization modeling, this transition might exist in gas with such high column densities and high ionizations as found in Table 6.

For observation CN, some lines detected blindly were tentatively identified as blueshifted lines with three different ranges of values (see Figure 10), as shown by the z_{out} column in Table 7. Taking into account errors on the energy of the line and its width, and taking also into account that the actual shape of the line may be different from a Gaussian curve (like for radiative recombination continuum), we found a velocity in emission v_{em} that is consistent with the value and error bars found when fitting the data with XSTAR models, i.e., $v_{\text{em}} = -0.098$ to $-0.050c$. This is also the case for the velocity in absorption of the second wind $v_{\text{abs2}} = -0.512$ to $-0.436c$, with absorption lines from Fe XXV He α , Fe XXVI Ly α , Fe XXVI Ly β , and Ni XXVIII Ly α , and the lower significance Si XIV Ly α line. The velocity of the first wind determined using photoionization models, $v_{\text{abs1}} = -0.319$ to $-0.264c$, is consistent with the identification of absorption lines Fe XXV He α , Fe XXVI Ly α , S XVI Ly α , Ne X Ly α , and Ni XXVIII Ly α . However, the lines tentatively identified as Fe XXVI Ly β , Fe XVII 2p-3d, O VIII Ly α (detected only at lower significance), O VIII Ly β , and Ne IX He α show a slightly higher velocity of -0.355 to $-0.332c$. This is consistent with the fact that the Fe XXVI Ly β absorption line of the first wind was not detected significantly when fitting the data with sets of Fe K lines (see Section 3.3). However, this Fe XXVI Ly β transition may contribute to the broad absorption feature around 11 keV. The O VIII and Ne IX He α absorption lines modeled by our broadband fitting with `warmabs` come mostly from the partially covering absorber. In our model, we chose to tie the velocity of this partial covering component to the one of the slowest UFO, consistently with Nardini et al. (2015), to improve its constraint when fitting the data. Furthermore, we also linked the turbulent velocities for the same reason. The photoionization modeling thus tended to make these O VIII and Ne IX lines broader than when detected during the blind line search, it can thus explain the slight difference of blueshift for these lines, and it suggests that the partially covering component may have a slightly different velocity than the slowest UFO.

For observation XN, some lines were tentatively identified in the spectrum above 5 keV, consistent with the identification for observation CN (see Table 8 and Figure 11). Owing to the large widths of the detected lines, several transitions can be attributed to the same line because they contribute to the absorption feature. Considering the uncertainties, the blueshift values resulting from this identification are close to the values resulting from the photoionization modeling (see Table 6). The slight difference could be due to the fact that the blind line search has been made only above 5 keV, while the

Table 7
Blind Line Search, Performed above 0.4 keV, on Observation CN

E_{rest}	σ	EW (eV)	ΔC	ID	E_{lab}	z_{out}
$0.69^{+0.001}_{-0.002}$	$0.005^{+0.0059}_{-0.0019}$	220.00 ± 164.00	30.39	O VIII Ly α (v_{em})	0.65	$-0.058^{+0.009}_{-0.005}$
$0.94^{+0.004}_{-0.004}$	$0.007^{+0.0043}_{-0.0032}$	15.90 ± 6.99	9.43	O VIII edge/rrc (v_{em})	0.87	$-0.074^{+0.008}_{-0.007}$
$1.04^{+0}_{-0.089}$	$0.001^{+0.001}_{-0}$	6.52 ± 2.80	8.10			
$1.06^{+0.001}_{-0}$	$0.001^{+0.0017}_{-0.0004}$	5.57 ± 2.78	6.71			
$1.10^{+0.004}_{-0.001}$	$0.001^{+0.0006}_{-0}$	-5.95 ± 1.55	9.01	O VIII Ly β (v_{abs1} , pc)	0.77	$-0.300^{+0.003}_{-0.001}$
$1.19^{+0.001}_{-0.001}$	$0.001^{+0.0013}_{-0.0001}$	-2.95 ± 0.98	7.08	Fe XVII 2p-3d (v_{abs1} , pc)	0.83	$-0.303^{+0.001}_{-0.001}$
$1.31^{+0.003}_{-0}$	$0.005^{+0.0021}_{-0.0021}$	-5.34 ± 1.09	7.19	Ne IX He α (v_{abs1} , pc)	0.92	$-0.298^{+0.003}_{-0.001}$
$1.37^{+0.001}_{-0.001}$	$0.002^{+0.0013}_{-0.001}$	-2.78 ± 0.90	6.48	Ne X Ly α (v_{abs1} , pc)	1.02	$-0.255^{+0.001}_{-0.001}$
$1.76^{+0.001}_{-0.001}$	$0.001^{+0.0008}_{-0}$	1.93 ± 0.77	6.93			
$1.84^{+0.001}_{-0.001}$	$0.001^{+0.0009}_{-0.0004}$	3.08 ± 1.23	12.18			
$2.93^{+0.003}_{-0.002}$	$0.001^{+0.0031}_{-0}$	7.24 ± 3.15	6.70	Si XIV edge/rrc (v_{em})	2.67	$-0.089^{+0.002}_{-0.001}$
$3.59^{+0.003}_{-0.005}$	$0.002^{+0.0014}_{-0.0006}$	-9.77 ± 3.15	7.52	S XVI Ly α (v_{abs1})	2.62	$-0.270^{+0.001}_{-0.001}$
$5.37^{+0.008}_{-0.002}$	$0.001^{+0.0535}_{-0.0002}$	17.50 ± 5.75	8.26			
$5.80^{+0.032}_{-0.056}$	$0.071^{+0.0297}_{-0.0426}$	49.60 ± 20.90	10.71			
$5.96^{+0.009}_{-0.014}$	$0.006^{+0.0087}_{-0.0025}$	-42.10 ± 0.11	11.52			
$6.91^{+0.003}_{-0.337}$	$0.600^{+0}_{-0.0528}$	238.00 ± 22.40	92.71	Fe XXV He α (v_{em})	6.70	$-0.030^{+0.000}_{-0.058}$
				+Fe XXVI Ly α (v_{em})	6.97	$0.009^{+0.000}_{-0.060}$
$9.11^{+0.238}_{-0.425}$	$0.434^{+0.1607}_{-0.426}$	-169.00 ± 0.00	7.74	Fe XXV He α (v_{abs1})	6.70	$-0.265^{+0.031}_{-0.076}$
				+Fe XXVI Ly α (v_{abs1})	6.97	$-0.235^{+0.052}_{-0.079}$
$11.34^{+0.075}_{-0.082}$	$0.016^{+0.146}_{-0.0065}$	-112.00 ± 0.00	8.94	Fe XXV He α (v_{abs2})	6.70	$-0.409^{+0.011}_{-0.005}$
				+Fe XXVI Ly α (v_{abs2})	6.97	$-0.385^{+0.012}_{-0.005}$
				+Fe XXVI Ly β (v_{abs1})	7.88	$-0.305^{+0.013}_{-0.005}$
				+Ni XXVIII Ly α (v_{abs1})	8.11	$-0.285^{+0.014}_{-0.006}$
$13.76^{+0.061}_{-0.1}$	$0.024^{+0.0783}_{-0.0158}$	-161.00 ± 0.62	6.88	Fe XXVI Ly β (v_{abs2})	7.88	$-0.427^{+0.006}_{-0.005}$
				+Ni XXVIII Ly α (v_{abs2})	8.11	$-0.411^{+0.006}_{-0.005}$
$15.18^{+0.127}_{-0.633}$	$0.349^{+0.2506}_{-0.0781}$	-28.30 ± 16.10	7.18			

Table 8
Blind Line Search, Performed above 5 keV, on Observation XN

E_{rest}	σ	EW (eV)	$\Delta\chi^2$	ID	E_{lab}	z_{out}
$7.19^{+0.069}_{-0.068}$	$0.549^{+0.050}_{-0.055}$	124.64 ± 10.84	124.90	Fe XXV He α (v_{em})	6.70	$-0.068^{+0.015}_{-0.016}$
				+ Fe XXVI Ly α (v_{em})	6.97	$-0.031^{+0.016}_{-0.017}$
$9.22^{+0.066}_{-0.082}$	$0.317^{+0.031}_{-0.023}$	-174.48 ± 7.62	208.38	Fe XXV He α (v_{abs1})	6.70	$-0.273^{+0.008}_{-0.008}$
				+Fe XXVI Ly α (v_{abs1})	6.97	$-0.244^{+0.008}_{-0.009}$
$11.24^{+0.069}_{-0.131}$	$0.593^{+0.007}_{-0.091}$	-173.50 ± 25.12	58.42	Fe XXVI Ly β (v_{abs1})	7.88	$-0.299^{+0.005}_{-0.014}$
				+ Ni XXVIII Ly α (v_{abs1})	8.11	$-0.278^{+0.005}_{-0.015}$
				+Fe XXV He α (v_{abs2})	6.70	$-0.404^{+0.004}_{-0.012}$
				+Fe XXVI Ly α (v_{abs2})	6.97	$-0.449^{+0.004}_{-0.012}$
$12.64^{+0.062}_{-0.154}$	$0.005^{+0.003}_{-0.003}$	-45.17 ± 23.88	6.79			
$13.62^{+0.063}_{-0.065}$	$0.009^{+0.002}_{-0.002}$	-106.03 ± 25.86	18.15	Fe XXVI Ly β (v_{abs2})	7.88	$-0.422^{+0.003}_{-0.003}$
				+ Ni XXVIII Ly α (v_{abs2})	8.11	$-0.405^{+0.003}_{-0.003}$

photoionization model takes the broadband spectrum into account. The determination of the velocities is thus more precise in the later case.

For observation C, only some emission lines and absorption lines from one UFO were identified. The blueshifted Fe XXV He α and Fe XXVI Ly α absorption features detected in the other observations were not detected, but some other lines (Si XIV

and S XVI) coming from the slowest UFO (and from the partially covering wind that is set to have the same velocity in our photoionization model) were identified, as shown in Table 9 and Figure 12. Some emission lines were also tentatively identified. The velocities derived from these identifications are globally consistent with the velocity values resulting from photoionization modeling (see Table 6).

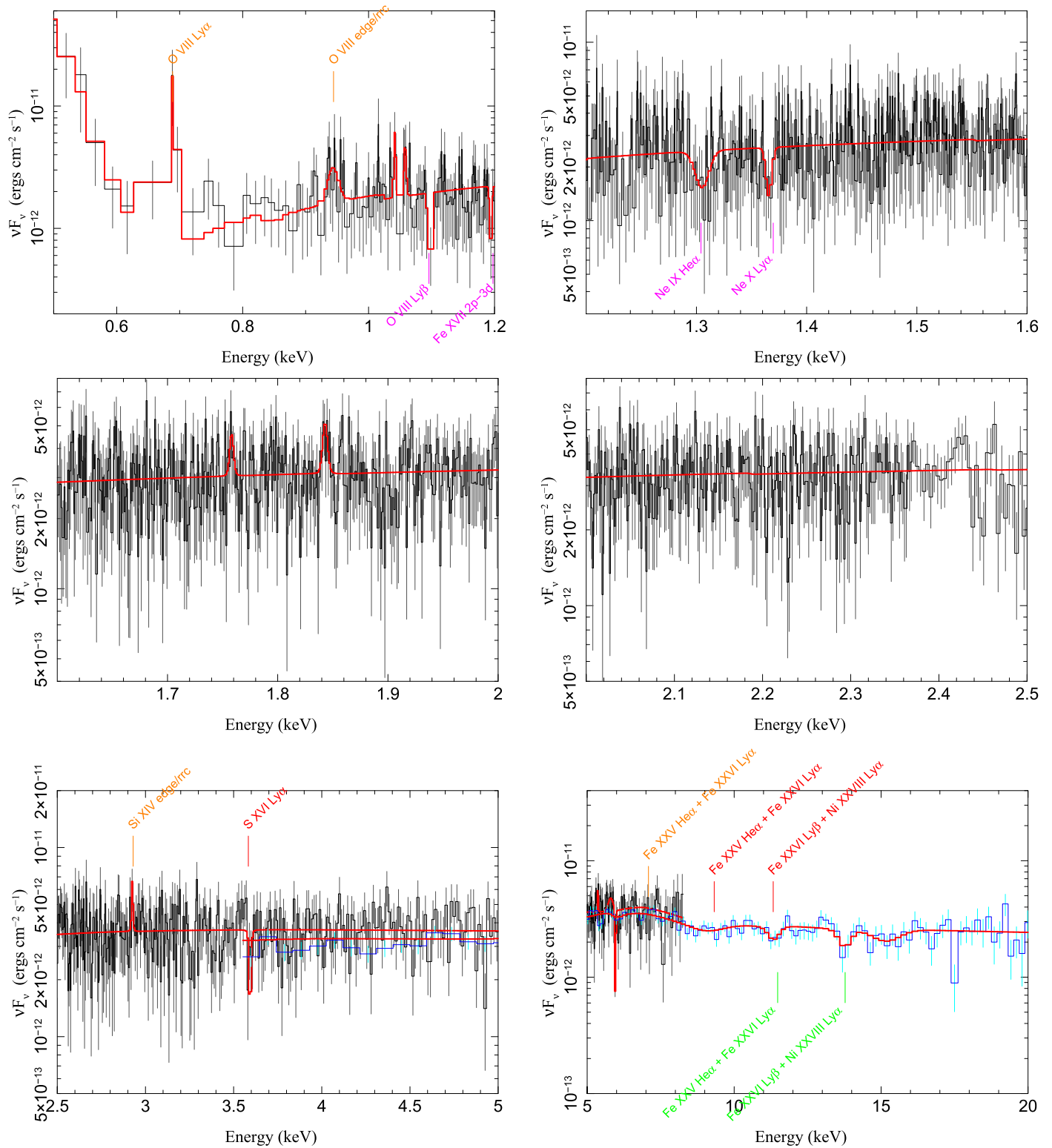


Figure 10. Result of the blind line search described in Section 5 for observation CN (entire spectrum). Some lines have been identified in concordance with results from the fitting with photoionization models described in Section 3.5. Orange lines come from photoemission, pink absorption lines come mostly from the partial covering absorber, red lines come from the first UFO (with the lowest velocity), and green lines come from absorption by the faster UFO.

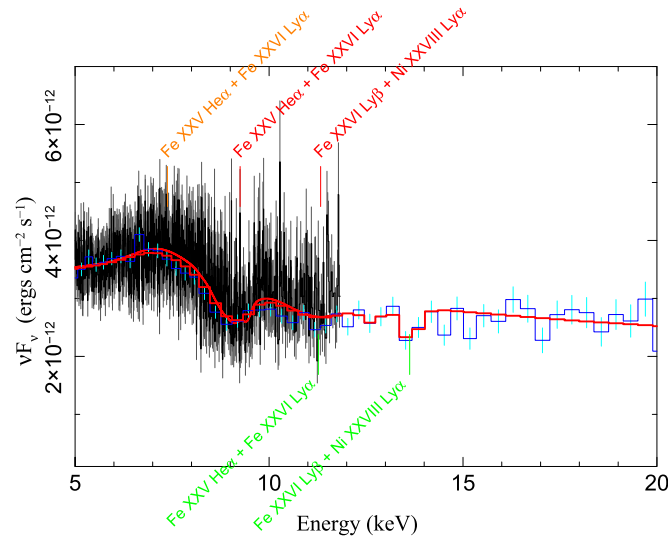


Figure 11. Result of the blind line search described in Section 5 for observation XN (hard spectrum), similarly to Figure 10.

Table 9
Blind Line Search, Performed above 0.4 keV, on Observation C

E_{rest}	σ	EW (eV)	ΔC	ID	E_{lab}	z_{out}
$0.76^{+0.005}_{-0.005}$	$0.008^{+0.0074}_{-0.0069}$	-16.8 ± 37.7	8.88	O VII He α (v_{abs1} , pc)	0.57	$-0.250^{+0.012}_{-0.012}$
$0.87^{+0.001}_{-0.003}$	$0.001^{+0.0005}_{-0}$	-5.34 ± 0.96	6.98	O VIII Ly α (v_{abs1} , pc)	0.65	$-0.253^{+0.001}_{-0.003}$
$0.88^{+0.002}_{-0.002}$	$0.004^{+0.0021}_{-0.0012}$	9.97 ± 4.09	11.01	O VIII edge/rrc (v_{em})	0.87	$-0.011^{+0.005}_{-0.004}$
$1.25^{+0.042}_{-0.022}$	$0.102^{+0.0302}_{-0.0258}$	-23.90 ± 0.00	32.53	Ne IX He α (v_{abs1} , pc) +Ne X Ly α (v_{abs1} , pc)	0.92 1.02	$-0.264^{+0.040}_{-0.029}$ $-0.184^{+0.045}_{-0.032}$
$1.31^{+0}_{-0.001}$	0.001^{+0}_{-0}	3.80 ± 0.02	8.54			
$1.39^{+0.001}_{-0.001}$	$0.002^{+0.0009}_{-0.0006}$	3.64 ± 1.64	7.68	Ne X edge/rrc (v_{em})	1.36	$-0.022^{+0.001}_{-0.001}$
$1.47^{+0.001}_{-0.001}$	$0.002^{+0.0013}_{-0.001}$	-3.66 ± 1.28	8.50			
$1.93^{+0.001}_{-0.001}$	$0.001^{+0.0011}_{-0}$	-2.67 ± 0.82	7.18			
$2.22^{+0.215}_{-0.064}$	$0.204^{+0.086}_{-0.1517}$	14.30 ± 8.07	9.55			
$2.45^{+0.003}_{-0.003}$	$0.004^{+0.0036}_{-0.0029}$	-5.98 ± 6.81	6.43			
$2.55^{+0.001}_{-0.001}$	0.001^{+0}_{-0}	7.03 ± 2.76	8.35			
$2.60^{+0.002}_{-0.001}$	$0.001^{+0.0004}_{-0}$	-6.46 ± 1.91	8.97	Si XIV Ly α (v_{abs1})	2.01	$-0.227^{+0.0007}_{-0.0003}$
$2.65^{+0.001}_{-0.001}$	$0.001^{+0.0023}_{-0}$	10.30 ± 4.00	9.51			
$3.08^{+0.002}_{-0.002}$	0.001^{+0}_{-0}	-8.23 ± 0.17	6.64			
$3.21^{+0.004}_{-0.004}$	$0.001^{+0.0112}_{-0}$	11.30 ± 4.63	8.51			
$3.47^{+0.192}_{-0.007}$	$0.033^{+0.1709}_{-0}$	-22.60 ± 32.80	9.84	S XVI Ly α (v_{abs1})	2.62	$-0.245^{+0.071}_{-0.002}$
$3.55^{+0.003}_{-0.328}$	$0.001^{+0.0004}_{-0.0003}$	-9.47 ± 1.06	6.26			
$3.92^{+0.004}_{-0.004}$	$0.005^{+0.0063}_{-0.0039}$	-11.70 ± 25.40	10.76			
$5.69^{+0.005}_{-0.005}$	$0.003^{+0.0035}_{-0.001}$	-23.40 ± 0.00	7.91			
7.03^{+0}_{-0}	$0.002^{+0.0225}_{-0.0007}$	54.90 ± 39.00	7.14	Fe XXV He α (v_{em})	6.70	$-0.047^{+0.003}_{-0.0001}$
$7.35^{+0.017}_{-0.01}$	$0.013^{+0.027}_{-0.0125}$	90.30 ± 80.00	11.03	Fe XXVI Ly α (v_{em})	6.97	$-0.052^{+0.006}_{-0.0029}$

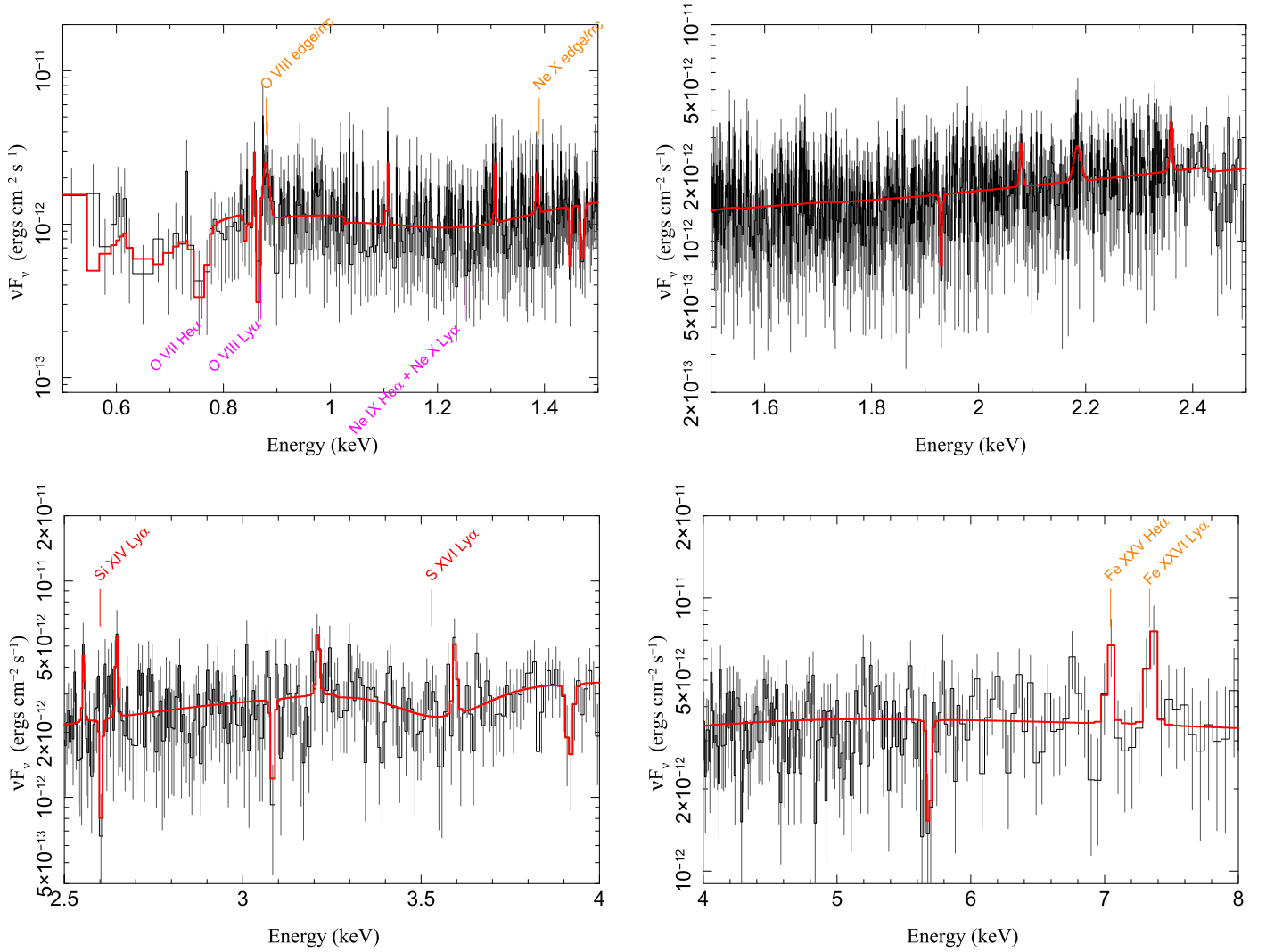


Figure 12. Result of the blind line search described in Section 5 for observation C (entire spectrum), similarly to Figure 10.

Appendix B Additional Kinematic Diagnostic

An additional diagnostic for identifying unknown kinematics of the absorbers, as proposed by Danekhar et al. (2018) in PG 1211 + 143, is to take the first-order *Chandra*/HETGS counts, and use the lines tentatively identified in Tables 7 and 9 as a set of reference wavelengths, to transform the grid repeatedly to velocities, resulting in Figure 13 for observations CN and C.

We can see that velocity values resulting from photoionization modeling (orange zone: emission, red zone: absorption from the slowest UFO, and green zone: absorption from the fastest UFO for observation CN alone) are consistent (considering the uncertainties) with the peaks of emission and absorption at certain velocities (black vertical lines) for both observations CN and C. This analysis provides an additional confirmation of the kinematic components of the UFO detected in PDS 456.

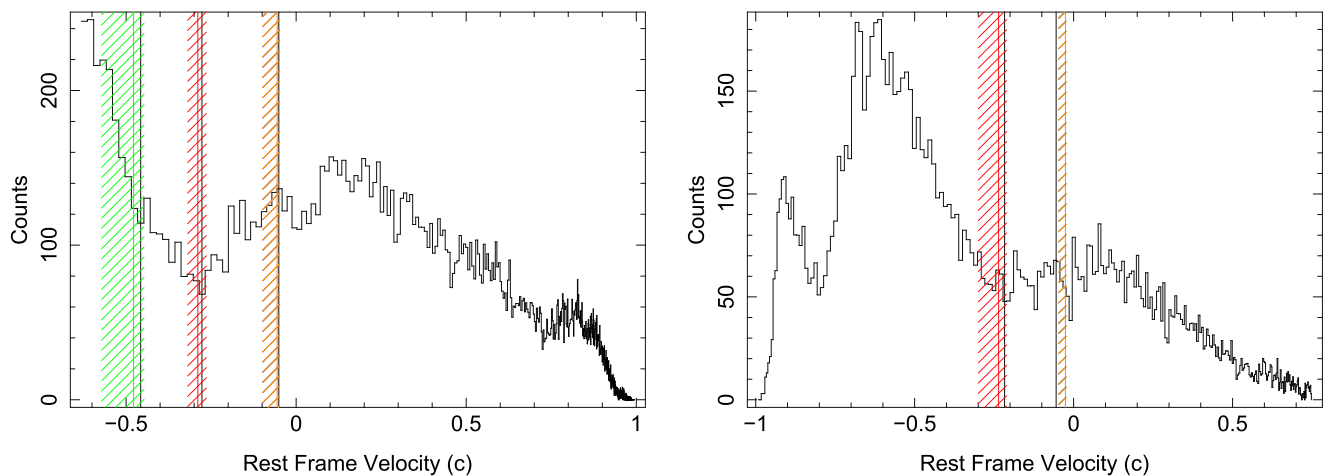



Figure 13. *Chandra*/HETGS first-order detector counts transformed in velocity bins centered on the identified lines in Tables 7 and 9. Left: observation CN. Right: observation C. Emission and absorption peaks consistent with photoionization results are indicated with black vertical lines. Velocity values resulting from photoionization modeling are also plotted for comparison (orange zone: emission, red zone: absorption from UFO 1, and green zone: absorption from UFO 2).

ORCID iDs

Rozenn Boissay-Malaquin  <https://orcid.org/0000-0003-2704-599X>

Ashkbiz Danehkar  <https://orcid.org/0000-0003-4552-5997>

Herman L. Marshall  <https://orcid.org/0000-0002-6492-1293>

Michael A. Nowak  <https://orcid.org/0000-0001-6923-1315>

References

- Alexander, D. M., & Hickox, R. C. 2012, *NewAR*, 56, 93
- Arnaud, K., Smith, R., & Siemiginowska, A. 2011, *Handbook of X-ray Astronomy* (Cambridge: Cambridge Univ. Press)
- Begelman, M. C., McKee, C. F., & Shields, G. A. 1983, *ApJ*, 271, 70
- Behar, E., Kaspi, S., Reeves, J., et al. 2010, *ApJ*, 712, 26
- Blandford, R. D., & Payne, D. G. 1982, *MNRAS*, 199, 883
- Blustin, A. J., Page, M. J., Fuerst, S. V., Branduardi-Raymont, G., & Ashton, C. E. 2005, *A&A*, 431, 111
- Breiman, L. 1973, *Statistics. With a View Toward Applications* (Boston, MA: Houghton Mifflin Co.)
- Canizares, C. R., Davis, J. E., Dewey, D., et al. 2005, *PASP*, 117, 1144
- Cash, W. 1979, *ApJ*, 228, 939
- Chakravorty, S., Kembhavi, A. K., Elvis, M., & Ferland, G. 2009, *MNRAS*, 393, 83
- Chakravorty, S., Petrucci, P.-O., Ferreira, J., et al. 2016, *A&A*, 589, A119
- Chartas, G., Brandt, W. N., & Gallagher, S. C. 2003, *ApJ*, 595, 85
- Chartas, G., Brandt, W. N., Gallagher, S. C., & Garmire, G. P. 2002, *ApJ*, 579, 169
- Chartas, G., Hamann, F., Eracleous, M., et al. 2014, *ApJ*, 783, 57
- Chiang, C.-Y., Cackett, E. M., Zoghbi, A., et al. 2017, *MNRAS*, 472, 1473
- Crenshaw, D. M., Kraemer, S. B., & George, I. M. 2003, *ARA&A*, 41, 117
- Dadina, M., Vignali, C., Cappi, M., et al. 2018, *A&A*, 610, L13
- Danehkar, A., Nowak, M. A., Lee, J. C., et al. 2018, *ApJ*, 853, 165
- Di Matteo, T., Springel, V., & Hernquist, L. 2005, *Nature*, 433, 604
- Dickey, J. M., & Lockman, F. J. 1990, *ARA&A*, 28, 215
- Done, C., Sobolewska, M. A., Gierliński, M., & Schurch, N. J. 2007, *MNRAS*, 374, L15
- Fabian, A. C. 2012, *ARA&A*, 50, 455
- Ferrarese, L., & Merritt, D. 2000, *ApJL*, 539, L9
- Fiore, F., Feruglio, C., Shankar, F., et al. 2017, *A&A*, 601, A143
- Fruscione, A., McDowell, J. C., Allen, G. E., et al. 2006, *Proc. SPIE*, 6270, 62701V
- Fukumura, K., Kazanas, D., Contopoulos, I., & Behar, E. 2010, *ApJ*, 715, 636
- Fukumura, K., Kazanas, D., Shrader, C., et al. 2018a, *ApJ*, 853, 40
- Fukumura, K., Kazanas, D., Shrader, C., et al. 2018b, *ApJL*, 864, L27
- Fukumura, K., Tombesi, F., Kazanas, D., et al. 2015, *ApJ*, 805, 17
- Gabriel, C., Denby, M., Fyfe, D. J., et al. 2004, in *ASP Conf. Ser.* 314, *Astronomical Data Analysis Software and Systems (ADASS) XIII*, ed. F. Ochsenbein, M. G. Allen, & D. Egret (San Francisco, CA: ASP), 759
- Gallo, L. C., & Fabian, A. C. 2013, *MNRAS*, 434, L66
- Garmire, G. P., Bautz, M. W., Ford, P. G., Nousek, J. A., & Ricker, G. R., Jr. 2003, *Proc. SPIE*, 4851, 28
- Gebhardt, K., Bender, R., Bower, G., et al. 2000, *ApJL*, 539, L13
- Gofford, J., Reeves, J. N., Braitto, V., et al. 2014, *ApJ*, 784, 77
- Gofford, J., Reeves, J. N., Tombesi, F., et al. 2013, *MNRAS*, 430, 60
- Grevesse, N., & Sauval, A. J. 1998, *SSRv*, 85, 161
- Hagino, K., Odaka, H., Done, C., et al. 2015, *MNRAS*, 446, 663
- Hagino, K., Odaka, H., Done, C., et al. 2016, *MNRAS*, 461, 3954
- Hamann, F., Chartas, G., Reeves, J., & Nardini, E. 2018, *MNRAS*, 476, 943
- Hopkins, P. F., & Elvis, M. 2010, *MNRAS*, 401, 7
- Houck, J. C. 2002, in *High Resolution X-ray Spectroscopy with XMM-Newton and Chandra*, ed. G. Branduardi-Raymont (London: MSSL), 17
- Huenemoerder, D. P., Mitschang, A., Dewey, D., et al. 2011, *AJ*, 141, 129
- Kaastra, J. S., Kriss, G. A., Cappi, M., et al. 2014, *Sci*, 345, 64
- Kalberla, P. M. W., Burton, W. B., Hartmann, D., et al. 2005, *A&A*, 440, 775
- Kallman, T., & Bautista, M. 2001, *ApJS*, 133, 221
- Kallman, T. R., Bautista, M. A., Goriely, S., et al. 2009, *ApJ*, 701, 865
- Kallman, T. R., Liedahl, D., Osterheld, A., Goldstein, W., & Kahn, S. 1996, *ApJ*, 465, 994
- Kallman, T. R., Palmeri, P., Bautista, M. A., Mendoza, C., & Krolik, J. H. 2004, *ApJS*, 155, 675
- King, A., & Pounds, K. 2015, *ARA&A*, 53, 115
- King, A. R. 2010, *MNRAS*, 402, 1516
- King, A. R., & Pounds, K. A. 2003, *MNRAS*, 345, 657
- Kormendy, J., & Ho, L. C. 2013, *ARA&A*, 51, 511
- Kraemer, S. B., Tombesi, F., & Bottorff, M. C. 2018, *ApJ*, 852, 35
- Krolik, J. H., & Kriss, G. A. 2001, *ApJ*, 561, 684
- Krolik, J. H., McKee, C. F., & Tarter, C. B. 1981, *ApJ*, 249, 422
- Lamers, H. J. G. L. M., Cerruti-Sola, M., & Perinotto, M. 1987, *ApJ*, 314, 726
- Lanzuisi, G., Giustini, M., Cappi, M., et al. 2012, *A&A*, 544, A2
- Lee, J. C., Kriss, G. A., Chakravorty, S., et al. 2013, *MNRAS*, 430, 2650
- Lobban, A. P., Pounds, K., Vaughan, S., & Reeves, J. N. 2016, *ApJ*, 831, 201
- Luminari, A., Piconcelli, E., Tombesi, F., et al. 2018, *A&A*, 619, A149
- Markert, T. H., Canizares, C. R., Dewey, D., et al. 1994, *Proc. SPIE*, 2280, 168
- Matzeu, G. A., Reeves, J. N., Braitto, V., et al. 2017a, *MNRAS*, 472, L15
- Matzeu, G. A., Reeves, J. N., Nardini, E., et al. 2016a, *AN*, 337, 495
- Matzeu, G. A., Reeves, J. N., Nardini, E., et al. 2016b, *MNRAS*, 458, 1311
- Matzeu, G. A., Reeves, J. N., Nardini, E., et al. 2017b, *MNRAS*, 465, 2804
- McKernan, B., Yaqoob, T., & Reynolds, C. S. 2007, *MNRAS*, 379, 1359
- Mehdipour, M., Kaastra, J. S., Kriss, G. A., et al. 2015, *A&A*, 575, A22
- Nardini, E., Reeves, J. N., Gofford, J., et al. 2015, *Sci*, 347, 860
- Nomura, M., & Ohsuga, K. 2017, *MNRAS*, 465, 2873
- O'Brien, P. T., Reeves, J. N., Simpson, C., & Ward, M. J. 2005, *MNRAS*, 360, L25
- Parker, M. L., Reeves, J. N., Matzeu, G. A., Buisson, D. J. K., & Fabian, A. C. 2018, *MNRAS*, 474, 108
- Piconcelli, E., Jimenez-Bailón, E., Guainazzi, M., et al. 2005, *A&A*, 432, 15
- Pounds, K. A., Reeves, J. N., King, A. R., et al. 2003, *MNRAS*, 345, 705

- Proga, D., & Kallman, T. R. 2004, *ApJ*, 616, 688
- Protassov, R., van Dyk, D. A., Connors, A., Kashyap, V. L., & Siemiginowska, A. 2002, *ApJ*, 571, 545
- Reeves, J. N., Braitto, V., Gofford, J., et al. 2014, *ApJ*, 780, 45
- Reeves, J. N., Braitto, V., Nardini, E., et al. 2016, *ApJ*, 824, 20
- Reeves, J. N., Braitto, V., Nardini, E., et al. 2018a, *ApJ*, 867, 38
- Reeves, J. N., Braitto, V., Nardini, E., et al. 2018b, *ApJL*, 854, L8
- Reeves, J. N., O'Brien, P. T., Braitto, V., et al. 2009, *ApJ*, 701, 493
- Reeves, J. N., O'Brien, P. T., Vaughan, S., et al. 2000, *MNRAS*, 312, L17
- Reeves, J. N., O'Brien, P. T., & Ward, M. J. 2003, *ApJL*, 593, L65
- Reeves, J. N., Wynn, G., O'Brien, P. T., & Pounds, K. A. 2002, *MNRAS*, 336, L56
- Reynolds, C. S., & Fabian, A. C. 1995, *MNRAS*, 273, 1167
- Silk, J., & Rees, M. J. 1998, *A&A*, 331, L1
- Sim, S. A., Proga, D., Miller, L., Long, K. S., & Turner, T. J. 2010, *MNRAS*, 408, 1396
- Strüder, L., Briel, U., Dennerl, K., et al. 2001, *A&A*, 365, L18
- Tombesi, F., Cappi, M., Reeves, J. N., et al. 2010, *A&A*, 521, A57
- Tombesi, F., Cappi, M., Reeves, J. N., et al. 2011, *ApJ*, 742, 44
- Tombesi, F., Cappi, M., Reeves, J. N., et al. 2013, *MNRAS*, 430, 1102
- Tombesi, F., Meléndez, M., Veilleux, S., et al. 2015, *Nature*, 519, 436
- Torres, C. A. O., Quast, G. R., Coziol, R., et al. 1997, *ApJL*, 488, L19
- Turner, T. J., & Miller, L. 2009, *A&ARv*, 17, 47
- Turner, T. J., Miller, L., Kraemer, S. B., & Reeves, J. N. 2011, *ApJ*, 733, 48
- Vignali, C., Comastri, A., Nicastro, F., et al. 2000, *A&A*, 362, 69
- Vignali, C., Iwasawa, K., Comastri, A., et al. 2015, *A&A*, 583, A141
- Wilks, S. S. 1938, *Ann. Math. Statist.*, 9, 60
- Wilms, J., Allen, A., & McCray, R. 2000, *ApJ*, 542, 914
- Yang, J., An, T., Zheng, F., et al. 2019, *MNRAS*, 482, 1701